U. Walzer, R. Hendel, and J. Baumgardner. Whole-mantle convection, continent generation, and preservation of geochemical heterogeneity. In W. E. Nagel, D. Kröner, and M. Resch, editors, High Perf. Comp. Sci. Engng. '07, pages 603-645. Berlin, 2008.

# Whole-Mantle Convection, Continent Generation, and Preservation of Geochemical Heterogeneity

Uwe Walzer[1], Roland Hendel[1], and John Baumgardner[2]

[1] Institut für Geowissenschaften, Friedrich-Schiller-Universität, Burgweg 11, 07749 Jena, Germany u.walzer@uni-jena.de
[2] Dept. Earth Planet. Science, University of California, Berkeley, CA 94720, USA

**Summary.** The focus of this paper is numerical modeling of crust-mantle differentiation. We begin by surveying the observational constraints of this process. The present-time distribution of incompatible elements are described and discussed. The mentioned differentiation causes formation and growth of continents and, as a complement, the generation and increase of the depleted MORB mantle (DMM). Here, we present a solution of this problem by an integrated theory that also includes the thermal solid-state convection in a 3-D compressible spherical-shell mantle heated from within and slightly from below. The conservation of mass, momentum, energy, angular momentum, and of four sums of the number of atoms of the pairs $^{238}$U-$^{206}$Pb, $^{235}$U-$^{207}$Pb, $^{232}$Th-$^{208}$Pb, $^{40}$K-$^{40}$Ar is guaranteed by the used equations. The pressure- and temperature-dependent viscosity is supplemented by a viscoplastic yield stress, $\sigma_y$. No restrictions are supposed regarding number, size, form and distribution of continents. Only oceanic plateaus touching a continent have to be united with this continent. This mimics the accretion of terranes. The numerical *results* are an episodic growth of the total mass of the continents and acceptable courses of the curves of the laterally averaged surface heat flow, *qob*, the Urey number, $Ur$, and the Rayleigh number, $Ra$. In spite of more than 4500 Ma of solid-state mantle convection, we typically obtain *separate*, although not simply connected geochemical mantle reservoirs. None of the reservoirs is free of mixing. This is a big step towards a reconciliation of the stirring problem. As expected, DMM strongly predominates immediately beneath the continents and the oceanic lithosphere. Apart from that, the result is a marble-cake mantle but DMM prevails in the upper half of the mantle. We find Earth-like continent distributions in a central part of $Ra$-$\sigma_y$ plot obtained by a comprehensive variation of parameters. There are also $Ra$-$\sigma_y$ areas with small deviations of the calculated total continental volume from the observed value, with acceptable values of $Ur$ and with realistic surface heat flow. It is remarkable that all of these different acceptable $Ra$-$\sigma_y$ regions share a common overlap area. We compare the observed present-time topography spectrum and the theoretical flow spectrum $n^{1/2} \times (n+1)^{1/2} \times \langle v^2_{n,pol} \rangle$.

## 1 Introduction: Whole-Mantle Convection and Geochemistry

Solid state convection currently explains the thermal evolution of the Earth and the plate-tectonic regime in a satisfying manner (*Schubert et al.* [94]). How well the Earth's chemical evolution is accounted for has not been so clear. Chemical differentiation alters the distribution of radioactive elements and volatiles and generates geochemical heterogeneity. On the other hand, convection diminishes and annihilates chemical heterogeneities by stirring in low-viscosity regions. Convection recycles the oceanic crust and transports and mixes mantle lithosphere into the deeper mantle. Mixing is suppressed and chemical signatures tend to be preserved, on the other hand, where mantle viscosity is high. Generation, preservation and destruction of heterogeneities are obviously influenced by the interplay between chemical differentiation, convection and secular cooling of the Earth's mantle. Only the present existence of remnants of the primordial mantle is a controversial question. It is evident that the chemical evolution of the mantle cannot be modeled without accounting for the convective process and the mixing it generates. On the other hand, the fact that chemical differentiation causes the distribution of heat-producing elements in the mantle to be non-uniform, no doubt, influences convection. This paper seeks to account for both differentiation and convecting/mixing together. We check our overall model against reality by comparing the evolution of continents, oceanic plateaus and of the MORB source that we obtain in our models with observations.

Modern seismic techniques document convincingly that subducted oceanic lithosphere penetrates into the lower mantle. Other seismic methods give strong support to the conclusion that at least some hotspots rise upward and penetrate the 660-km phase boundary (*Van der Hilst et al.* [109], *Grand et al.* [39]). Moreover, differential travel times may be used to determine the vertical distance between the olivine-wadsleyite discontinuity and the ringwoodite-perovskite discontinuity and its lateral variation. From this it has been deduced that at least some hotspots penetrate the 660-km boundary (*Bina* [14]). At the corresponding places, a thinning of the transition zone thickness has been observed as expected from corresponding Clausius-Clapeyron slopes (*Schubert et al.* [94], chapter 4.6.2). It is evident that the topography of the mentioned seismic discontinuities can be explained by thermal perturbations of phase transformations in a peridotite mantle (*Helffrich and Wood* [44]). There are also direct evidences of plumes penetrating the 660-km discontinuity by seismic tomography. These studies demonstrate that the transition zone is not impermeable either for slabs or for plumes. Tomography suggests that some plumes originate in the D″ layer. Other plumes probably originate from shallower depths, e.g., near the 660-km discontinuity (*Courtillot et al.* [29], *Montelli et al.* [75]).

Some have proposed that the *bulk* compositions of the upper and the lower mantle are different, especially in the Mg/Fe and Mg/Si ratios, and that the

660-km discontinuity is not only a phase transition from ringwoodite to perovskite plus magnesiowüstite and from majorite garnet to Al-bearing Mg-rich perovskite (*Hirose* [46]) but also a discontinuity in the *major-element* abundances. *Jackson and Rigden* [55] showed, however, that the essential features of the seismological models can be well explained by the phase transitions of a pyrolite model, as a special case, and that, in the general case, the current knowledge of the seismic structure of the mantle is consistent with a *uniform major-element* composition of the mantle with the probable exception of the D″ layer. From a geochemical point of view, *Palme and O'Neill* [80] concluded that, concerning the major elements, the whole Earth's mantle is compositionally uniform if we consider averages of large volumes. If the abundances, normalized to Ti and CI, are drawn versus equidistant locations of the carbonaceous chondrites CI, CM, CO, CK, CV and the Earth's mantle, then constant-value lines result for Al and Ca and monotonously decreasing curves arise from this procedure for other major and moderately volatile elements. So, the Earth's mantle may be considered as an extension of the carbonaceous chondrite trend. Only the Cr content is too low in the present mantle as a result of Cr partitioning into the outer core. *Bina* [14] also concluded that the seismic arguments for a chemical boundary of the major elements at the 660-km discontinuity have faded. An isochemical mantle is consistent with seismic results. However, this conclusion applies only for the major elements since it is these elements that constrain the bulk physical parameters such as compressional velocity and density which can be computed for a perfect lattice. Major elements are the essential constituents of rock-forming minerals. Trace elements often act only as tracers (*Hofmann* [50]). However, other important physical quantities such as shear viscosity, seismic shear velocity, electrical conductivity, etc. depend on the concentrations of Schottky holes, Frenkel defects and dislocations which, in turn, strongly depend on small amounts of volatiles. Also small concentrations of U, Th and K influence the heating rate and hence the buoyancy that drives convection. To summarize this introduction, we conclude that there is strong evidence for whole-mantle convection. In regard to the *major elements*, averaging over large volumes, current evidence points to a chemically homogeneous mantle except for the lithosphere and its counterpart at CMB, the D″ layer. It is quite possible that this simple picture may have to be modified somewhat since *Trampert et al.* [106] showed that compositional variation affects the seismic velocities, $v_p$ and $v_s$, not only in the D″ layer but also in most of the lowermost mantle.

## 2 Observational Constraints

### 2.1 The Evolution of Continents, the MORB Source and Other Possible Geochemical Reservoirs

#### Geochemical Preliminary Examinations

The continental crust (CC) (*Hofmann* [48], *McCulloch and Bennett* [71], *Rudnick and Gao* [91]) is extraordinarily enriched in incompatible elements compared to the bulk silicate earth (BSE). Therefore it is to be expected that there are one or more regions in the mantle that are depleted in incompatible elements in a complementary manner. Mid-oceanic ridge basalt (MORB) is supplied by a source region that has to be situated immediately below the oceanic lithosphere since, independently where oceanic plates are spreading apart, MORB is surprisingly homogeneous in its trace element composition. This source region appears to be very well stirred in comparison to that of ocean-island basalts (OIB). *Allègre and Lewin* [4] emphasize the homogeneity of MORB. Let $R/R_A$ denote the mass ratio $^3$He/$^4$He of rock divided by the present-day $^3$He/$^4$He value of the atmosphere. *Barfod et al.* [8] showed that the $R/R_A$ values of ridge basalts are around 8 with a small standard deviation. HIMU-like OIBs have lower $R/R_A$ values with greater standard deviations. Nearly all *other* OIBs have augmented $R/R_A$ ratios with large standard deviations. However, *Hofmann* [50] pointed out that also the depleted MORB mantle (DMM) is isotopically not entirely uniform.

*Hofmann* [50] reported a fundamental observation: The abundances of the elements Rb, Pb, U, Th, K, Ba, La, Nb, Sr, Na, Yb, Al, Ca, Si, Sc, Mn, Co and Mg, normalized by their BSE abundances (*McDonough and Sun* [73]) have been plotted versus their degree of compatibility for three reservoirs: continental crust (*Rudnick and Fountain* [90]), MORB (*Su* [99]), and DMM. If the generation of CC would be a one-act differentiation process then the result could be easily explained as follows: The more incompatible an element is the stronger it is enriched in CC since it rose within the melt to this place. DMM is the complementary mantle part where the abundances of the most incompatible elements have the lowest values. If this depleted mantle region is again partly melted, the differentiation product is a typically oceanic crust (MORB) with an observed normalized concentration curve of the mentioned elements that is between the CC and the DMM curve. So compared to DMM, the MORB curve is also somewhat enriched.

However, the formation of CC is not a single-stage process, but a multi-stage process. The enrichment of CC happens by three kinds of processes: (a) partial melting in the uppermost parts of the mantle and ascent into the oceanic crust, (b) dehydration and decarbonation in subduction zones with metasomatic transport (*Hofmann*, [50]), and (c) generation of plateau basalts. The source rocks for plateau basalts are relatively enriched parts of the mantle that penetrated into the uppermost mantle layer that has now usually a

DMM composition. Plateau basalts are divided into three classes: continental flood basalts, oceanic plateaus and ocean basin flood basalts (*Coffin and Eldholm* [25]). The latter two classes of large igneous provinces (LIP) are driven near the continental margin by the conveyor-belt-like oceanic lithosphere and accreted to the continent in the zones of andesitic volcanism. Generation of LIPs is episodically distributed over the time axis of the Earth's history. LIP volcanism was dominant during the Alpidic orogenesis, in contrast to the MORB volcanism in the orogenetically somewhat more quiet period of today. On other terrestrial planets of our solar system, LIP volcanism appears to be the dominant form. A terrestrial example is the Ontong Java Plateau. Its basalt developed from a 30% melting of a peridotite source. It can only be achieved by decompression of hot material with a potential temperature >1500°C beneath a thin oceanic lithosphere. As expected, the Ontong Java Plateau basalt is enriched in U, Th and K in comparison to Pacific MORB. It is also isotopically and chemically distinct from it (*Fitton et al.* [34]).

Furthermore, the present-day proportion of DMM of the mass of the mantle is not exactly known since it depends on which element is used and on its assumed abundance in CC and DMM. If samarium and neodymium are not so extremely enriched in CC, then smaller volumes of DMM would be sufficient. 50% of depleted mantle is derived from Cs, Rb, Th and K. *Bennett* [10] estimated that between 30% and 60% of the mantle is depleted if an intermediate degree of depletion of DMM is assumed. *Hofmann* [50] deduced a depleted reservoir of the mantle between 30% and 80%. *Van Keken et al.* [110], however, itemized some strong arguments against the opinion that the rest of the mantle is simply a BSE reservoir. *Hofmann et al.* [51] investigated the mass ratio Nb/U of MORB and IOB and found a very similar average. The same conclusion applies for Ce/Pb. *Rudnick and Fountain* [90] derived Nb/U=47±11 for MORBs, Nb/U=52±15 for OIBs but Nb/U=8 for CC. The trace element ratios Ce/Pb, Nb/U, and Nd/U proved to be nearly identical for MORB and OIB and to be nonprimitive, i.e., there is no correspondence with BSE. Evidently, it is not possible to derive the BSE abundances simply from the MORB and OIB abundances. Some authors concluded from the observations that there is no present-day primordial material at all in the mantle. However, *Hofmann* [50] emphasized that only mass ratios of similarly incompatible pairs of elements are suitable for addressing this issue.

When the isotope ratio of a single element is plotted against the isotope ratio of another element, for many basaltic rocks from around the world, including OIBs and MORBs, they tend to scatter into distinct mixing lines. At each end of such a line is an extremal case. If, for example, the present-day mass ratio of $^{206}Pb/^{204}Pb$ is plotted versus $^{87}Sr/^{86}Sr$ then four distinctly separated mixing lines typically appear, the ends of which are called HIMU, DMM, EM1 and EM2 (cf. *Hofmann* [50], Fig. 15). HIMU stands for high $\mu$ where $\mu = (^{238}U/^{204}Pb)_{\tau=0}$ (*Houtermans* [53], *Zindler and Hart* [124]). $\tau$ is the age. One interpretation is that these end compositions represent only extremes of a continuum of mixtures of isotopic compositions that are dis-

tributed on various spatial scales throughout the mantle. The other opinion is that these end-member compositions represent separate distinct reservoirs in different regions of the mantle. However, the observed compositions are *not* evenly distributed in $^{206}Pb/^{204}Pb$–$^{87}Sr/^{86}Sr$ space. Instead, four linear trends dominate. Not only this observation but also the following hint by *Hofmann* [49] argues for the second option, namely that nearly pure HIMU basalts are found not only in a single ocean island group like the Cook-Austral chain but also on St.Helena on the other side of the globe. The latter argument is not invalidated by the fact that Mangaia, an individual island of the Cook chain, is distinctly different from the observed HIMU of the other Cook-Austral islands and St. Helena (*Stracke et al.* [98]). HIMU has not been observed in MORB and is rare in OIB. It could represent ancient recycled oceanic crust (*Stracke et al.* [98]). EM1 and EM2 are more enriched in very incompatible elements compared to HIMU. EM2 shows maximum $^{87}Sr/^{86}Sr$ values at nearly constant $^{206}Pb/^{204}Pb \approx 19$ whereas EM1 forms a distinctly separated line beneath the EM2 line and is distinctly separated regarding $^{206}Pb/^{204}Pb$. The usual explanation for EM1 is that it is generated by recycling of oceanic crust plus portions of lower CC or subcontinental lithosphere or ancient pelagic sediments. EM2 is customarily explained by recycling of oceanic crust with portions of the upper CC (*Willbold and Stracke* [116]). The latter authors deny the distinction between EM1 and EM2. They propose a flowing transition and explain the common EM by subduction of oceanic crust with variable proportions of lower and upper CC.

If all mixing arrays are plotted, e.g. in a three-dimensional $^{206}Pb/^{204}Pb$–$^{87}Sr/^{86}Sr$–$^{143}Nd/^{144}Nd$ diagram then all mixing lines aim at a small volume called FOZO (or focal zone) according to *Hart et al.* [42]. There are also related proposals: PREMA (*Wörner et al.* [118], *Zindler and Hart* [124]), PHEM (*Farley et al.* [33]) and C (*Hanan and Graham* [41]). FOZO is significantly more radiogenic in lead isotopes than DMM, moderately more radiogenic in Sr and less radiogenic in Nd and Hf (*Hofmann* [50]). Furthermore, FOZO has a higher $^{208}Pb/^{206}Pb$ ratio than HIMU. Although FOZO is evidently produced by subduction and is by no means primordial, FOZO can play the part of the rich principal reservoir in our present convection-differentiation model, rich in U, Th and K. There would be a broad mixing zone between the FOZO and the DMM reservoir. FOZO would be the main source in the OIBs while EM1, EM2 and HIMU represent contributions from minor reservoirs. The latter ones have not to be joined to one region each. The different contributions of the various minor reservoirs generate the large isotopic and chemical standard deviations of OIBs, large in comparison to that of MORBs. *Stracke and Hofmann* [98] redefined a new FOZO that is similar to the traditional FOZO according to *Hart et al.* [42]. They propose that this new FOZO could be a ubiquitously dispersed, small-scale component in the entire mantle. We remark that, according to our present dynamical model, the percentage of FOZO in the upper half of the mantle should be less than in the lower half.

This result corresponds with *Wilson's and Spencer's* [117] conclusion that FOZO is the characteristic signal of lower mantle plumes.

Geochemical models that *totally* abandon the assumption of BSE remnants in the present-day mantle are unable to explain the observation that the flux of $^3$He is unidirectional, that, e.g., Reykjanes Ridge has a $^3$He content 15 times higher than that of DMM and that the averaged $^3$He concentration in the plume sources is 4 times higher than that of DMM. *Hilton and Porcelli* [45] are convinced that at present 1039-2270 mol·a$^{-1}$ primordial $^3$He leaves the Earth. *Trieloff and Kunz* [107] systematically discuss the problem of noble gases in the Earth's mantle. One proposal for the source of primordial noble gases has been the Earth's core (*Tolstikhin and Marty* [104], *Porcelli and Halliday* [85]). This proposal is unconvincing since the viscosity of the outer core is between 1 and 100 Pa·s and it circulates with velocities between 10 and 30 km/a. So, each volume element of the outer core has been in frequent contact with the CMB during the Earth's evolution: If the mantle is unable to retain its $^3$He, then the outer core cannot retain its inventory either. But for the dynamical theory, presented in this paper, it is irrelevant where exactly the $^3$He source region is situated. It is only important that there are regions within the present mantle which have higher abundances of U, Th and K than occur in the DMM. MORBs and OIBs are chemically distinct and their standard deviations are different. So, it is improbable that both of them originate from the same quasi-homogeneous DMM.

Moreover, the present-day heat output of the mantle is 36 TW: it is not possible to produce such a large amount of heat from a mantle that is entirely a DMM reservoir (*Bercovici and Karato* [12]). A more detailed argument is as follows: The Earth's present-day heat loss is 44 TW (*Pollak et al.* [83]). 4.8-9.6 TW of it are produced by the CC (*Taylor and McLennon* [102], *Rudnick and Fountain* [90]), *Porcelli and Ballentine* [84]). The different numbers stem from different assumptions on the average CC abundances of radioactive elements. The contribution of the Earth's core is between 3 and 7 TW (*Buffet et al.* [18]. If the DMM abundances would be by a factor of 1/2.6 lower than the BSE abundances according to *Jochum et al.* [56] then a whole-mantle DMM would generate only 7.2 TW (*Porcelli and Ballentine* [84]). The contribution of secular cooling is between 21.8 TW and 17.8 TW. If the terms of CC, the core and secular cooling are subtracted from the observed 44 TW then values between 9.6 and 14.4 TW remain. The latter numbers exceed the 7.2 TW of a hypothetical mantle that is comprised entirely of pure DMM. Therefore, the mantle must contain at least one reservoir that is enriched in U, Th and K.

## Continental Crust: Massive Early Formation or Gradual or Episodic Growth?

The isotopic compositions of lunar rocks (*Norman et al.* [77]) and of SNC meteorites (*Brandon et al.* [17], *Nyquist et al.* [78], *Bogard et al.* [15]) show rapid chemical differentiation of Moon and Mars within the first 200 Ma of

their existence. Therefore it is highly probable that not only did an iron core form early but a silicate crust did as well. It has been argued that not only the Moon but also the Earth posessed a magma ocean early in their histories (*Stevenson* [97], *Tonks and Melosh* [105]). In the case of the Earth, it is not clear whether all or only part of the mantle was melted. The generation of the metallic cores likely occured within the first 30 Ma associated with the decay of short-lived isotopes (*Cameron* [23], *Kleine et al.* [65]). It was a controversial question whether the total mass of the Earth's crust continued to grow during its later evolution taking no account of the mentioned early stage. *Armstrong* [6] and *Bowring and Housh* [16] advocated that the full amount of current mass of CC formed very early, before an age of 4 Ga. They assumed that CC has only been recycled since that time. On the other hand, there is strong evidence that juvenile CC has indeed been formed during the Earth's subsequent evolution. Therefore, models involving episodic or continuous continental growth have been proposed (*Taylor and McLennon* [102], *McCulloch and Bennett* [71, 72], *Condie* [28], *Bennett* [10]). The $^{147}$Sm–$^{143}$Nd isotopic system and the $^{176}$Lu–$^{176}$Hf decay both suggest that chemical differentiation of CC has persisted over the whole of geological history in addition of a pulse of differentiation during the Earth's earliest history (*Bennett* [10]).

The of Sm/Nd ratio was not altered during the accretion of the Earth since both elements are refractory. Neither was this ratio modified during core formation since both elements are lithophile. Both conclusions also apply for Lu/Hf. Therefore, we may conclude that these two ratios in BSE are chondritic. However, the quantity $\varepsilon_{Nd}$ as a function of time displays an ongoing chemical evolution of DMM distributed over the whole $\geq 4.49 \times 10^9\, a$ history of the solid silicate mantle. Here
$\varepsilon_{Nd} = \left[(^{143}Nd/^{144}Nd_{(t)sample})/(^{143}Nd/^{144}Nd_{(t)BSE}) - 1\right] \times 10^4$
with $t$ the crystallization age. $\varepsilon_{Nd}$ of the depleted mantle appears to have increased non-uniformly, probably episodically, and reaches its maximum value of $\varepsilon_{Nd} = 10 \pm 2$ for the present epoch (*Hofmann* [50]). Observed isotopic compositions of Nd point strongly to complex processes of depletion and crustal recycling. Similarly, the increase of $\varepsilon_{Hf}$ of DMM leads to the same conclusion. Here $\varepsilon_{Hf} = \left[(^{176}Hf/^{177}Hf_{(t)sample})/(^{176}Hf/^{177}Hf_{(t)BSE}) - 1\right] \times 10^4$. The quantity $\varepsilon_{Hf}$ increases non-uniformly and reaches its present value of $\varepsilon_{Hf} = 16 \pm 4$ (*Salters and White* [92], *Vervoort and Blichert-Toft* [111], *Amelin et al.* [5], *Bennett* [10]). A similar non-uniform evolution can be shown for the $^{187}$Os/$^{188}$Os ratio using mantle-derived samples. *Condie* [28] further demonstrated a progressive increase in the Nb/Th ratio for the depleted mantle throughout the Earth's history. If we now consider the problem of CC evolution as it relates to the mantle components DMM, FOZO, HIMU, DM1 and DM2, discussed in Section 2.1. then we must infer that these components developed by different differentiation processes, subduction and convective stirring. Also if we view the problem from this perspective it seems improbable that CC formed exclusively during the Earth's initial history. Subduction continuously entrains heterogeneous material that subsequently sinks to the

bottom of the mantle. The composition of this basal layer almost certainly changes with time (*Davies* [31], *Gurnis* [40], *Coltice and Ricard* [26], *Albarède and Van der Hilst* [2]). *Arndt* [7] provides a review of similar and alternative views of the mantle's chemical evolution.

### 2.2 Further Observational Constraints

In contrast with the other terrestrial planets, the Earth has a pronounced double-peaked hypsometric curve. This relatively sharp division of the surface of the solid Earth into continents and ocean basins reflects a contrast in chemical composition. The thickness of the oceanic crust is only 0-7 km whereas the continental crust is distinctly thicker. Its thickness depends on its age: Archaic CC, older than $2.5 \times 10^9 a$, has an average thickness of 41 km whereas Early Proterozoic CC that is older than $1.6 \times 10^9 a$ has an average thickness of 43 km. Late Proterozoic and Phanerozoic CC has a mean thickness of 35 km. The continental lithospheric mantle, attached to the CC, has essentially the same age. Isotopic investigations of the continental lithospheric mantle show that it has been isolated from the convecting mantle since the corresponding time of CC formation (*Kramers* [66], *Pearson et al.* [82]). There are, of course, alterations due to metasomatism (*Alard et al.* [1], *Burton et al.* [22]). The oceanic lithosphere moves in a piecewise plate-like manner and subducts. That is why there is no oceanic plate older than Upper Jurassic. Therefore, the upper CC is the only extensively accessible record of information on the main part of the Earth's history. Only relatively small parts of the continent record have been removed by subduction or by delamination of the continental lithospheric mantle.

*Reymer and Schubert* [87] summarized continental crustal growth curves of different authors and presented their own continuous growth curve. *Taylor and McLennon* [102] emphasized what they recognize as major episodes of crustal growth. *Condie* [28] also emphasizes the episodicity of this process. *O'Nions and Tolstikhin* [79] show that convective avalanches could be responsible for episodic crustal growth. It is plausible that episodicity in convection indirectly causes the episodes of growth of CC. *Yuen and Malevsky* [123] and *Yuen et al.* [122] pointed out that mantle convection can operate in the hard turbulence regime at early stages of planetary thermal evolution and subside to a present-day state of soft turbulence. It is also to be expected that the rate of chemical differentiation depends directly on mantle convection. So, if convection displays episodes of vigor the juvenile contributions to the continents should also be episodic. Finally, we mention the process of the intracrustal differentiation that generates two chemically heterogeneous reservoirs with distinct systematic differences in their abundances of incompatible elements, namely, the upper and lower CC (*Rudnick and Gao* [91]). Table B.1 of *Walzer et al.* [113] specifies essential differences between the Earth and terrestrial planets.

# 3 Model

## 3.1 Balance of Mass, Momentum and Energy

We use a numerical strategy for modeling the differentiation and mixing processes that have operated during our planet's history. We solve the differential equations of infinite Prandtl-number convection using a three-dimensional finite-element spherical-shell method. These express the conservation of mass, momentum, and energy. The mass balance

$$\frac{\partial \rho}{\partial t} + \bigtriangledown \cdot (\rho \mathbf{v}) = 0 \tag{1}$$

with the anelastic-liquid approximation simplifies to

$$\bigtriangledown \cdot \mathbf{v} = -\frac{1}{\rho}\mathbf{v} \cdot \bigtriangledown \rho \tag{2}$$

where $\rho$ is density, $t$ time, and $\mathbf{v}$ is velocity.

The conservation of momentum can be written as

$$\rho \left( \frac{\partial \mathbf{v}}{\partial t} + \mathbf{v} \cdot \bigtriangledown \mathbf{v} \right) = - \bigtriangledown P + \rho \mathbf{g} + \frac{\partial}{\partial x_k} \tau_{ik} \tag{3}$$

where $P$ is the pressure, $\mathbf{g}$ is the gravity acceleration, and $\tau_{ik}$ is the deviatoric stress tensor. For spherical symmetry, we have $\mathbf{g} = -g\mathbf{e}_r$ and the hydrostatic pressure gradient may be written as

$$-\frac{\partial P}{\partial r} = \rho g \tag{4}$$

By definition $K_S = -V \left(\frac{\partial P}{\partial V}\right)_S$ and $\frac{V}{V_0} = \frac{\rho_0}{\rho}$, where $K_S$ is the adiabatic bulk modulus, $V$ volume, $S$ entropy, $r$ the radial distance from the Earth's center. Hence

$$K_S = \rho \left( \frac{\partial P}{\partial \rho} \right)_S = \rho \left( \frac{\partial P}{\partial r} \right)_S \left( \frac{\partial r}{\partial \rho} \right)_S \tag{5}$$

Substituting Eq. (4) into Eq. (5) we obtain

$$\left( \frac{\partial \rho}{\partial r} \right)_S = \frac{-\rho^2 g}{K_S} \tag{6}$$

Upon neglecting horizontal spatial variations in $\rho$, Eqs. (2) and (6) yield

$$\bigtriangledown \cdot \mathbf{v} = -\frac{1}{\rho}\mathbf{v} \cdot \bigtriangledown \rho \cong -\frac{1}{\rho} v_r \frac{\partial \rho}{\partial r} = \frac{\rho g v_r}{K_S} \tag{7}$$

It is well-known that

$$K_S = \frac{c_p}{c_v} K_T = (1 + \alpha \gamma_{th} T) K_T \tag{8}$$

where $K_T$ is the isothermal bulk modulus, $c_p$ the specific heat at constant pressure, $c_v$ the specific heat at constant volume, $\alpha$ the coefficient of thermal expansion, $\gamma_{th}$ the thermodynamic Grüneisen parameter and $T$ the absolute temperature.

Eq. (3) can be rewritten as

$$\rho \frac{dv_i}{dt} = \rho g_i + \frac{\partial \sigma_{ki}}{\partial x_k} \tag{9}$$

Using this equation, the energy balance can be expressed as follows

$$\rho \frac{du}{dt} + \frac{\partial q_i}{\partial x_i} = Q + \sigma_{ik} \dot{\varepsilon}_{ik} \tag{10}$$

where $u$ is the specific internal energy, $Q$ is the heat generation rate per unit volume; $v_i$, $g_i$, $q_i$, $x_i$, $\sigma_{ik}$, $\dot{\varepsilon}_{ik}$ are the components of velocity, gravity acceleration, heat flow density, location vector, stress tensor and strain-rate tensor, respectively.

Another formulation of Eq. (10) is

$$\rho \left[ \frac{\partial}{\partial t} + \mathbf{v} \cdot \bigtriangledown \right] u = \bigtriangledown \cdot (k \bigtriangledown T) + Q - P \bigtriangledown \cdot \mathbf{v} + 2W_D \tag{11}$$

where

$$2W_D = \sigma_{ik} \dot{\varepsilon}_{ik} + P \bigtriangledown \cdot \mathbf{v} \tag{12}$$

and

$$q_k = -k \frac{\partial T}{\partial x_k} \tag{13}$$

The quantity $k$ denotes the thermal conductivity. Using

$$du = T\ ds - P\ dv \tag{14}$$

and

$$du = T \left( \frac{\partial s}{\partial T} \right)_P dT + T \left( \frac{\partial s}{\partial P} \right)_T dP - P dv \tag{15}$$

we eliminate the specific internal energy in Eq. (11) and obtain the equation

$$\rho c_p \frac{dT}{dt} = \bigtriangledown \cdot (k \bigtriangledown T) + Q + \alpha T \frac{dP}{dt} + 2W_D \tag{16}$$

since

$$c_p = T \left( \frac{\partial s}{\partial T} \right)_P \quad \text{and} \quad \left( \frac{\partial s}{\partial P} \right)_T = - \left( \frac{\partial v}{\partial T} \right)_P = -v\alpha \tag{17}$$

Here $s$ signifies the specific entropy, $v$ the specific volume, $c_p$ the specific heat at constant pressure and $\alpha$ the coefficient of thermal expansion.

Next, a less well known version of the energy balance is presented: Eq. (11) is equivalent to

$$\rho\left(\frac{du}{dt}+P\frac{dv}{dt}\right)=\tau_{ik}\frac{\partial v_i}{\partial x_k}+\bigtriangledown\cdot(k\bigtriangledown T)+Q \tag{18}$$

because of Eq. (2) and $\frac{1}{\rho}=v$.
Inserting Eq. (14) into Eq. (18), we obtain

$$\rho T\frac{ds}{dt}=\tau_{ik}\frac{\partial v_i}{\partial x_k}+\frac{\partial}{\partial x_j}\left(k\frac{\partial}{\partial x_j}T\right)+Q \tag{19}$$

On the other hand,

$$ds=\left(\frac{\partial s}{\partial T}\right)_v dT+\left(\frac{\partial s}{\partial v}\right)_T dv \tag{20}$$

and

$$\left(\frac{\partial s}{\partial T}\right)_v=\frac{c_v}{T}\,,\qquad \left(\frac{\partial s}{\partial v}\right)_T=\alpha K_T \tag{21}$$

This implies

$$Tds=c_v dT+\alpha K_T T d\left(\frac{1}{\rho}\right) \tag{22}$$

or

$$Tds=c_v dT-\frac{c_v\gamma T}{\rho}d\rho \tag{23}$$

where

$$\gamma_{th}=\frac{\alpha K_T}{c_v\rho} \tag{24}$$

stands for the thermodynamic Grüneisen parameter.

Inserting Eq. (23) into Eq. (19) we obtain

$$\rho c_v\frac{dT}{dt}-c_v\gamma T\frac{d\rho}{dt}=\tau_{ik}\frac{\partial v_i}{\partial x_k}+\frac{\partial}{\partial x_j}\left(k\frac{\partial}{\partial x_j}T\right)+Q \tag{25}$$

From Equations (1) and (25)

$$\rho c_v\frac{dT}{dt}=-\rho c_v\gamma T\frac{\partial v_j}{\partial x_j}+\tau_{ik}\frac{\partial v_i}{\partial x_k}+\frac{\partial}{\partial x_j}\left(k\frac{\partial}{\partial x_j}T\right)+Q \tag{26}$$

or

$$\frac{\partial T}{dt}=-v_j\frac{\partial}{\partial x_j}T-\gamma T\frac{\partial v_j}{\partial x_j}+\frac{1}{\rho c_v}\left(\tau_{ik}\frac{\partial v_i}{\partial x_k}+\frac{\partial}{\partial x_j}\left(k\frac{\partial}{\partial x_j}T\right)+Q\right] \tag{27}$$

or

$$\frac{\partial T}{\partial t}=-\frac{\partial(Tv_j)}{\partial x_j}-(\gamma-1)T\frac{\partial v_j}{\partial x_j}+\frac{1}{\rho c_v}\left(\tau_{ik}\frac{\partial v_i}{\partial x_k}+\frac{\partial}{\partial x_j}\left(k\frac{\partial}{\partial x_j}T\right)+Q\right] \tag{28}$$

This is an alternative formula for the *energy conservation*. Although $c_v$ appears in Eq. (28), the latter expression is equivalent to Eq. (16) where $c_p$ is used. The deviatoric stress tensor can be expressed by

$$\tau_{ik} = \eta \left( \frac{\partial v_i}{\partial x_k} + \frac{\partial v_k}{\partial x_i} - \frac{2}{3} \frac{\partial v_j}{\partial x_j} \delta_{ik} \right) \tag{29}$$

in the Eqs. (3) and (28), where $\eta$ denotes the viscosity.

As an *equation of state* we take

$$\rho = \rho_r \left[ 1 - \alpha(T - T_r) + K_T^{-1}(P - P_r) + \sum_{k=1}^{2} \Gamma_k \Delta\rho_k / \rho_r \right] \tag{30}$$

where the index $r$ refers to the adiabatic reference state, $\Delta\rho_k/\rho_r$ or $f_{ak}$ denotes the non-dimensional density jump for the $k$th mineral phase transition. $\Gamma_k$ is a measure of the relative fraction of the heavier phase where $\Gamma_k = \frac{1}{2}\left(1 + \tanh \frac{\pi_k}{d_k}\right)$ with $\pi_k = P - P_{0k} - \gamma_k T$ describing the excess pressure $\pi_k$. The quantity $P_{0k}$ is the transition pressure for vanishing temperature $T$. A non-dimensional transition width is denoted by $d_k$. The quantity $\gamma_k$ represents the Clausius-Clapeyron slope for the $k$th phase transition. $\Gamma_k$ and $\pi_k$ have been introduced by *Richter* [89] and *Christensen and Yuen* [24].
Because of the very high Prandtl number, the left-hand side of Eq. (3) vanishes. Hence, we use the following version of the equation of *conservation of momentum.*

$$0 = -\frac{\partial}{\partial x_i}(P - P_r) + (\rho - \rho_r) g_i(r) + \frac{\partial}{\partial x_k} \tau_{ik} \tag{31}$$

The final version of the equation of *conservation of mass* is

$$0 = \frac{\partial}{\partial x_j} \rho v_j \tag{32}$$

which stems from Eq. (2). The Equations (28), (30), (31) and (32) are a system of six scalar equations that we use to determine six scalar unknown functions, namely $T$, $\rho$, $P$ and the three components of $v_i$.

### 3.2 Viscosity and Phase Transitions

The viscosity law of this paper is presented as follows. Based on experimental results of *Karato and Li* [58], *Karato and Wu* [60] and *Li et al.* [68], a Newtonian solid-state creep is assumed for the Earth's mantle. The shear viscosity, $\eta$, is calculated by

$$\eta(r, \theta, \phi, t) = 10^{r_n} \cdot \frac{\exp(c\,\overline{T_m/T_{av}})}{\exp(c\,\overline{T_m/T_{st}})} \cdot \eta_3(r) \cdot \exp\left[ c_t \cdot T_m \left( \frac{1}{T} - \frac{1}{T_{av}} \right) \right] \tag{33}$$

where $r$ is the radius, $\theta$ the colatitude, $\phi$ the longitude, $t$ the time, $r_n$ the viscosity-level parameter, $T_m$ the melting temperature, $T_{av}$ the laterally averaged temperature, $T_{st}$ the initial temperature profile, $T$ the temperature as a function of $r, \theta, \phi, t$. The quantity $\eta_3(r)$ is the viscosity profile at the initial temperature and for $r_n = 0$. So, $\eta_3(r)$ describes the dependence of the

viscosity on pressure and on the mineral phase boundaries. The derivation of $\eta_3(r)$ is to be found in *Walzer et al.* [113]. The quantity $r_n$ has been used for a stepwise shift of the viscosity profile to vary the averaged Rayleigh number from run to run. The second factor of the right-hand side of Eq. (33) describes the increase of the viscosity profile with the cooling of the Earth. For $MgSiO_3$ perovskite we should insert c=14, for MgO wüstite c=10 according to *Yamazaki and Karato* [120]. So, the lower-mantle $c$ should be somewhere between these two values. For numerical reasons, we are able to use only c=7. In the lateral-variability term, we inserted $c_t = 1$. For the uppermost 285 km of the mantle (plus crust), an effective viscosity, $\eta_{eff}$, was implemented where

$$\eta_{eff} = \min\left[\eta(P,T), \frac{\sigma_y}{2\dot{\varepsilon}}\right] \tag{34}$$

The pressure is denoted by $P$, the second invariant of the strain-rate tensor by $\dot{\varepsilon}$. The quantity $\sigma_y$ is a viscoplastic yield stress.

The viscosity profile of the present paper (see Fig. 2) displays a high-viscosity lithosphere. Beneath of it is a low-viscosity asthenosphere down to the 410-km phase boundary. The transition zone is highly viscous, at least between 520 and 660 km depth. This model is corroborated by the fact that downgoing slabs extending down to the asthenosphere only show extensional fault-plane solutions. If a slab enters the transition zone then compressional focal mechanisms are observed (*Isacks and Molnar* [54]), also in the case that the 660-km discontinuity is not touched. These observations cannot be explained by the olivine-wadsleyite or the wadsleyite-ringwoodite phase transition since the Clausius-Clapeyron slopes for both are positive and the phase boundary distortion enhances the cold downflow in these cases. The increase of the number of seismic events per 20 km Bin beneath of 520 km depth (*Kirby et al.* [64]) can be explained by a viscosity increase. Only if the slab reaches the 660-km phase boundary the corresponding negative Clausius-Clapeyron slope can contribute to the observed compressional fault-plane solutions. If the slab penetrates the 660-km phase boundary then the latter is deflected somewhat downward. An earthquake has never been observed below that deflection. Beneath of that, the slab is only detectable by elevated densities and seismic compressional and shear velocities. Therefore it is reasonable to infer a low-viscosity layer in the uppermost part of the lower mantle (*Kido and Yuen* [62]). This proposal of a high-viscosity transition layer, that is embedded between two low-viscosity layers, is consistent with the proposition that the transition zone is composed mostly of garnet and spinel (*Meade and Jeanloz* [74], *Karato et al.* [59], *Karato* [57], *Allègre* [3]). If there are no further phase transitions in the lower mantle, except near the D″ layer (*Matyska and Yuen* [70]), then the viscosity must rise considerably as a function of depth because of the pressure dependence of the activation enthalpy of the prevailing creeping mechanism for regions where the temperature gradient is near to adiabatic. This implies a thick high-viscosity central layer in the lower mantle.

We infer a strong temperature gradient of the D″ layer which causes a strong decrease of viscosity in the near neighborhood above the CMB.

In our derivation of $\eta_3(r)$, however, we did *not* make use of the above arguments. They serve only as a corroboration. The alternative systematic derivation is described by *Walzer et al.* [113]. We start from a self-consistent theory using the Helmholtz free energy, the Birch-Murnaghan equation of state, the free-volume Grüneisen parameter and *Gilvarry's* [36] formulation of Lindemann's law. The viscosity is calculated as a function of melting temperature obtained from Lindemann's law. We use pressure, $P$, bulk modulus, $K$, and $\partial K/\partial P$ from the seismic model PREM (*Dziewonski and Anderson* [32]) to obtain the relative variation in radial viscosity distribution. To determine the absolute scale of the viscosity profile, we utilize the standard postglacial-uplift viscosity of the asthenosphere below the continental lithosphere.

Our $\eta_3(r)$ profile is supported by several recent studies. New inversion investigations for mantle viscosity profiles reveal an acceptable resolution down to 1200 km depth. For greater depths, models based on solid-state physics seem to be more reliable. *Kido and Čadek* [61] and *Kido et al.* [63] found two low-viscosity layers below all three oceans. The first layer is between the lithosphere and 410 km depth. The second one is between 660 and about 1000 km depth. *Panasyuk and Hager* [81] made a joint inversion of the geoid and the dynamic topography. They found three families of solutions for the radial viscosity profile that are different regarding the position of the lowest-viscosity region: (a) directly beneath the lithosphere, (b) just above 400 km depth or (c) just above 670 km depth. The results of *Forte and Mitrovica* [35] show even more similarity with our profile $\eta_3(r)$. Their viscous-flow models, based on two seismic models of three-dimensional mantle structure, revealed two viscosity maxima at about 800 and about 2000 km depth. This is similar to our model for $\eta_3(r)$ that has also two maxima in the interior although is has been derived by a completely different method. *Cserepes et al.* [30] investigated the effects of similar viscosity profiles on Cartesian 3-D mantle convection in a box.

In our dynamical model, we take into account the full effect of phase boundary distortion of the olivine-wadsleyite and of the ringwoodite-perovskite phase boundary. The input parameters that define these phase transitions are provided in Table 1.

### 3.3 Numerical Method and Implementation

In our models we include the full pressure dependence and the full radial temperature dependence of viscosity. For numerical reasons, however, we are able to treat only a part of the lateral temperature dependence of the viscosity. At the mineral phase boundaries in the interior of the Earth's mantle, there are not only discontinuities of the seismic velocities and of the density but also jumps of activation volumes, activation energies and, therefore, of activation enthalpies. Since the viscosity depends exponentially on the activation

**Table 1.** Model parameters

| Parameter | Description | Value | |
|---|---|---|---|
| $r_{min}$ | Inner radius of spherical shell | $3.480 \times 10^6$ | m |
| $r_{max}$ | Outer radius of spherical shell | $6.371 \times 10^6$ | m |
| | Temperature at the outer shell boundary | 288 | K |
| $h_1$ | Depth of the exothermic phase boundary | $4.10 \times 10^5$ | m |
| $h_2$ | Depth of the endothermic phase boundary | $6.60 \times 10^5$ | m |
| $\gamma_1$ | Clapeyron slope for the olivine-wadsleyite transition | $+1.6 \times 10^6$ | $\mathrm{Pa{\cdot}K^{-1}}$ |
| $\gamma_2$ | Clapeyron slope for the ringwoodite-perovskite transition | $-2.5 \times 10^6$ | $\mathrm{Pa{\cdot}K^{-1}}$ |
| $f_{a1}$ | Non-dimensional density jump for the olivine-wadsleyite transition | 0.0547 | |
| $f_{a2}$ | Non-dimensional density jump for the ringwoodite-perovskite transition | 0.0848 | |
| | Begin of the thermal evolution of the *solid* Earth's silicate mantle | $4.490 \times 10^9$ | a |
| $d_1$ | Non-dimensional transition width for the olivine-wadsleyite transition | 0.05 | |
| $d_2$ | Non-dimensional transition width for the ringwoodite-perovskite transition | 0.05 | |
| | Begin of the radioactive decay | $4.565 \times 10^9$ | a |
| $c_t$ | Factor of the lateral viscosity variation | 1 | |
| $k$ | Thermal conductivity | 12 | $\mathrm{W{\cdot}m^{-1}{\cdot}K^{-1}}$ |
| $nr + 1$ | Number of radial levels | 33 | |
| | Number of grid points | $1.351746 \times 10^6$ | |

enthalpy of the prevailing creeping process, the conclusion is inescapable that there are considerable viscosity jumps at the upper and lower surfaces of the transition zone. These jumps cause numerical problems in the solution of the balance equations. The problems have been solved. Nevertheless, our group is searching for more effective solutions of the numerical jump problem. The minor discontinuity at a depth of 520 km has been neglected.

We treat the mantle as a thick spherical shell. The grid for this domain is constructed by projection of the edges of a regular icosahedron onto concentric spherical shell surfaces with different radial distances from the center. These surfaces subdivide the mantle into thin shells. A first step of grid refinement consists of bisecting the edges of the resulting spherical triangles into equal parts. Connecting the new points with great circles, we obtain four smaller triangles from each starting triangle. The process can be repeated by successive steps to obtain a grid with the desired horizontal resolution. We replicate the resulting almost uniform triangular grid at different radii to generate the 3D grid for a spherical shell. We can use different formulae for the distribu-

tion of the radial distances of the spherical grid surfaces. In this paper, we used exclusively a radially nearly equidistant grid with a superposed sinoidal half-wave length to refine the grid near the upper and lower boundaries of the spherical shell. The grid is non-adaptive.

The Navier-Stokes equations as well as pressure and creeping velocity are discretized using finite elements. We apply piecewise linear basis functions for the creeping velocity and either piecewise constant or piecewise linear basis functions for the pressure. We solve the equations for pressure and velocity simultaneously by a Schur-complement conjugate-gradient iteration (*Ramage and Wathen* [86]). This is a further development of an Uzawa algorithm. We solve the energy equation using an iterative multidimensional positive-definite advection-transport algorithm with explicit time steps (*Bunge and Baumgardner* [20]). Within the Ramage-Wathen procedure, the resulting equation systems are solved by a multigrid procedure that utilizes radial line Jacobi smoothing. In the multigrid procedure, prolongation and restriction are handled in a matrix-dependent manner. In this way, it is possible to handle the strong variations and jumps of the coefficients associated with the strong viscosity gradients (*Yang* [121]). For the formulation of chemical differentiation, we modified a tracer module developed by Dave Stegman. This module contains a second-order Runge-Kutta procedure to move the tracer particles in the velocity field. Each tracer carries the abundances of the radionuclides. In this sense, tracers are active attributes which determine the heat production rate per unit volume that varies with time and position.

[30] The FORTRAN code is parallelized by domain decomposition and explicit message passing (MPI) (*Bunge* [19]). For the most runs, we used a mesh of 1351746 nodes. For some runs, we used a mesh of 10649730 nodes in order to check the convergence of the lower resolution runs. We found hardly any discernable differences ($<0.5\%$) for the Rayleigh number, the Nusselt number, the Urey number and the laterally averaged surface heat flow as a function of time. The calculations were performed on 32 processors of a Cray Strider Opteron cluster. The code was benchmarked for constant viscosity convection by *Bunge et al.* [21] with data of *Glatzmaier* [37] for Nusselt numbers, peak velocities, and peak temperatures. The result is a good agreement with deviations $\leq 1.5\%$.

### 3.4 Heating, Initial and Boundary Conditions, and Chemical Differentiation

We assume the Earth's mantle is heated mostly from within. This internal heating is expressed by the heat production density $Q$ in Eq. (28) that is measured in $\mathrm{W \cdot m^{-3}}$.

$$Q = H \cdot \rho \tag{35}$$

where $H$ is the specific heat production with

$$H = \sum_{\nu=1}^{4} a_{\mu\nu} a_{if\nu} H_{0\nu} \exp(-t/\tau_\nu) \tag{36}$$

Table 2 presents the parameter data we use for the four major heat-producing isotopes. Here, $\nu$ stands for the radionuclide in the formulae, $\tau_\nu$ represents the decay time or the 1/e life, $H_{o\nu}$ denotes the specific heat production of the $\nu$th radionuclide $4.565 \times 10^9$ years ago, $a_{if\nu}$ is the isotope abundance factor.

**Table 2.** Data of the major heat-producing isotopes

| Isotope | $^{40}$K | $^{232}$Th | $^{235}$U | $^{238}$U |
|---|---|---|---|---|
| $\nu$ | 1 | 2 | 3 | 4 |
| $\tau_\nu$[Ma] | 2015.3 | 20212.2 | 1015.4 | 6446.2 |
| $H_{0\nu}[Wkg^{-1}]$ | $0.272\times10^{-3}$ | $0.0330\times10^{-3}$ | $47.89\times10^{-3}$ | $0.1905\times10^{-3}$ |
| $a_{if\nu}$ | 0.000119 | 1 | 0.0071 | 0.9928 |

We represent the distribution of radionuclides in the mantle by tracers. Each tracer is associated with a specific geochemical principal reservoir. Because of mixing, the boundaries of these reservoirs become blurred with time. In principle, even a total mixing and homogenization of the mantle is possible if the dynamic system of the mantle allows this process. Each tracer is identified by a tracer index. The reservoir concentrations of elements are given by Table 3. The lower five elements of Table 3 serve only for the computation of concentration maps but not for the calculation of heating energy either because the contributions of these elements are too low or because they are daughter nuclides. Since the relative masses of HIMU, EM1 and EM2 are small they have been neglected in the *calculated* model, S3, of this paper. Our model mantle starts with a uniform distribution of exclusively type-1 tracers, i.e., we start with a pure BSE mantle. If the modeled temperature, $T$, approaches the melting temperature, $T_m$, in a certain volume then chemical differentiation takes place. Plateau basalts quickly rise to form the plateaus as a terrane or preliminary form of the continental crust (CC) leaving behind depleted MORB mantle (DMM). The numerical conditions for this simplified chemical differentiation process will be given below. We do not use a detailed melt extraction equation system like the 2-D code of *Schmeling* [93] since, for a 3-D spherical-shell code, this would require more computational resources than we currently have available.

We chose *McCulloch and Bennett* [71] reservoir abundances for our models because of the good internal compatibility of this geochemical model. These abundances are similar to those proposed by other investigators. *Heier* [43], *Taylor and McLennon* [102], *Hofmann* [48], *McCulloch and Bennett* [71], *Wedepohl* [115] and *Rudnick and Fountain* [90] have proposed values for the continental-crust K:U ratio of 10777, 10020, 10000, 10064, 10020, 11092, respectively.

**Table 3.** The abundances $a_{\mu\nu}$ of the major heat-producing elements

| Reservoir | Primordial mantle (ppm) | Oceanic crust [MORB] (ppm) | Continental crust (ppm) | Depleted MORB mantle (ppm) |
|---|---|---|---|---|
| tracer index | (1) | (2) | (3) | (4) |
| element | | | | |
| U | 0.0203 | 0.047 | 0.94 | 0.0066 |
| Th | 0.0853 | 0.12 | 4.7 | 0.017 |
| K | 250. | 600. | 9460. | 110. |
| Pb | 0.1382 | 0.30 | 7.0 | 0.035 |
| Sm | 0.4404 | 2.63 | 4.62 | 0.378 |
| Nd | 1.354 | 7.3 | 25.5 | 0.992 |
| Rb | 0.635 | 0.56 | 35.5 | 0.112 |
| Sr | 21.0 | 90. | 310. | 16.6 |

The spherical shell of our present model has free-slip and impermeable boundary conditions for both the Earth's surface and CMB. The upper surface is isothermal at 288 K. The CMB is also isothermal spatially, but not with respect to time. Applying a cooling core-mantle evolution model (*Steinbach et al.* [96]), we adjust the CMB temperature, $T_c$, after each time step according to the heat flow through the CMB. We assume a homogeneous core in thermodynamic equilibrium similar to the approaches of *Steinbach and Yuen* [95] and *Honda and Iwase* [52].

Prior to this work, our modeling efforts relating to the problem of integrated convection-fractionation were restricted to two dimensions (*Walzer and Hendel* [112], *Walzer et al.* [114]). We here describe two tracer methods for our 3-D compressible spherical-shell models. The first method has the advantage of being simple and readily comprehensible. The second method avoids certain deficiencies of the first one.

*The first method:* We assign a 3-D cell to each node in the icosahedral grid with 1351746 nodes. There are Type-1 tracers, Type-3 tracers and Type-4 tracers with the abundances given in Table 3. At the beginning of the evolution of the model, the shell contains exclusively Type-1 tracers. Each cell starts with eight tracers or 64 tracers, respectively. The tracers are carried along by the velocity field. The element concentration of a node is determined by the average $\overline{a_{\mu\nu}}$, of the abundances of the elements carried by the tracers in the cell associated with the node. A local tracer refresh (LTR) is applied if a cell has fewer than four (or 32) or more than twelve (or 96) tracers. Tracers are redistributed from or to the neighboring cells, respectively, using fixed prescriptions. This procedure is to prevent a cell becoming empty of tracers and therefore having $\overline{a_{\mu\nu}}$ become indeterminate. If the conditions for partial melting are fulfilled in a sufficiently large volume then the Type-1 tracers in that volume are converted to Type-4 tracers corresponding to DMM to mimic the depletion. A greater number of changed Type-1 tracers are necessary to produce one new Type-3 tracer (corresponding to CC) from a Type-1 tracer

near the surface above a region of differentiation, since the continental Type-3 tracers have considerably higher abundances of incompatible elements. The ratio $z_3^*$ is given by

$$z_3^* = (a_{\mu\nu}^{(3)} - a_{\mu\nu}^{(1)})/(a_{\mu\nu}^{(1)} - a_{\mu\nu}^{(4)}) \tag{37}$$

$$z_3 = \text{round } (z_3^*) \tag{38}$$

For uranium, $z_3^* = 67.131387$ based on the values of Table 3, and therefore $z_3 = 67$. The same integer is derived for thorium and potassium. So, 67 Type-1 tracers from the asthenosphere are necessary to generate one Type-3 tracer in the lithosphere by transformation of one Type-1 tracer at the corresponding place. If a cell (a) has more than 50% Type-1 tracers and is, therefore, fertile and (b) has fulfilled the condition $T > f_3 \cdot T_m$ in its grid point where $f_3$ is a fixed parameter with $0 < f_3 \leq 1$ and (c) has at least five neighboring cells with common boundary surfaces that also fulfill (a) and (b) then this cell is called Type-A cell. If a cluster of simply connected Type-A cells has $n_{thr}$ Type-1 tracers then the tracers are instantaneously changed in Type-4 tracers. This does not concern all of these tracers but $(n_{thr} + n_n \cdot z_3)$ of them where $n_n$ is an integer. Here *thr* stands for threshold. The center of gravity of the cluster is projected to the top surface of the shell. The corresponding point at the surface is called $P'$. A number of $(n_{thr}/z_3 + n_n)$ Type-1 tracers nearest to $P'$ and not deeper than 65 km are changed to Type-3 tracers. This corresponds to oceanic plateaus. All Type-3 tracers are unsinkable and move with the horizontal component of the velocity field. This rule mimics the tendency of the continents to resist subduction. If two Type-3 tracers approach each other nearer than a small distance $d_{in}$ then they are connected to a continent. If an unconnected Type-3 tracer approaches to a continent nearer then $d_{in}$ then it will be connected with the continent. Tracers that are connected to form a continent move with a common angular velocity, $\boldsymbol{\omega}$, associated with that continent around the center of the shell. This quantity $\boldsymbol{\omega}$ is calculated as the vector sum of the single angular velocities derived from the horizontal component of the undisturbed nodal velocity. Hence, the continent moves as a plate-like thin shell across the upper surface. In our present model, oceanic plates develop without any such construction simply as a result of the yield stress and of the existence of an asthenosphere.

*The second method:* The second method is a translation of the ideas of the first method to the Stegman code with some improvements. For the starting distribution of the tracers, a cell is attributed to each node. Tracers are initially distributed in an almost uniform manner about each grid point, with eight (or 64) tracers per grid-point cell, except for the grid-point cells on the top and bottom shell boundaries, which have four (or 32). A new feature of this second method is that each particle carries its initial mass as one of its attributes. The sum of the individual particle masses is equal to the total mass of the mantle. If 4 tracers are regularly distributed to each half-cell then the mass, *mip*, of a tracer, *ip*, is calculated by

$$mip = 1/4 * (volume\ of\ the\ half\text{-}cell) * (density\ of\ the\ node) \tag{39}$$

The mass, $M_{mantle}$, of the whole mantle results from

$$M_{mantle} = \sum_{ip=1}^{npm} mip \tag{40}$$

where $npm$ is the total number of tracers in the mantle.

A *memory cell* contains all tracers that are attributed to a node. Its base is a spherical hexagon or pentagon the corners of which are in the triangle centers of the triangular distribution around a node. Its altitude is again between the grid spherical surfaces $ir$ and $(ir + 1)$.

*Combining and splitting:* Material from the top boundary layer that sinks to the CMB experiences a density increase and an increase of the tracer number per volume up to a factor two. However, the cell volume is diminished by a factor four during a movement from the surface to the CMB. So, a reduction of the number of tracers per memory cell by a factor two is to be expected. If the tracer number falls below four (or 32) then each tracer of this cell is split into two tracers. The mass of such a tracer is distributed equally to the child tracers. The reverse process will occur during upwelling. Overcrowding of the memory cells can take place. For technical reasons, we limit the number of tracers per cell to 12 (or 96). Each tracer coming into the cell beyond this limit is combined with one of the other tracers according to their order in memory. The masses are added. The location of the new tracer is the center of gravity of the two annihilated tracers. Only tracers of the same type can be combined. If an excess tracer enters the cell with a type not present in the cell, then two tracers of the most abundant type are united, the first two in the storage sequence. Splitting or combining does not alter the cell mass, $Mc$, nor the sum of the tracer masses, $mipc$, present in the cell.

The base of an *interpolation cell* is a spherical hexagon or pentagon the corners of which are the lateral neighboring nodes. The upper and lower base is determined by the upper and lower neighboring grid spherical surfaces. All tracers inside the interpolation cell contribute to the interpolation of tracer attributes, e.g., elemental abundance, to the node. The nearer the tracer is to the grid point, the larger is the weighting factor. The lateral weighting factor, $wl$, is simply the barycentric coordinate of the tracer when the tracer and node are both radially projected onto the same spherical surface:

$$wl = (\alpha|\beta|\gamma)(ip) \tag{41}$$

The radial weighting factor is given by

$$\begin{aligned} wr &= \frac{(r(ir+1) - rip)}{(r(ir+1) - r(ir))} \quad \text{if } rip > r(ir) \\ wr &= \frac{(rip - r(ir-1))}{(r(ir) - r(ir-1))} \quad \text{if } rip \leq r(ir) \end{aligned} \tag{42}$$

where $r(ir+1|ir-1)$ are the neighboring grid spherical surfaces of the radius, $r(ir)$, of the node and $rip$ is the radius of the tracer. The total weighting factor is the product of these two factors.

$$wip = wr * wl \tag{43}$$

The weighted mass, $wmip$, of a tracer is

$$wmip = wip * mip \tag{44}$$

The mass, $wMc$, of an interpolation cell can be derived by a weighted integration over the mass continuum of the cell. This has to be done in such a way that

$$wMc(interpolation\ cell) = Mc(memory\ cell) \tag{45}$$

The total mass balance is not violated by the weighting procedure:

$$\begin{aligned}\sum_{c=1}^{nc}\sum_{ip=1}^{npc} wmipc &= \sum_{c=1}^{nc}\sum_{i3c=1}^{n3c}\sum_{ip3c=1}^{nip3c} wmip3c = \sum_{i3=1}^{n3}\sum_{ip3=1}^{nip3}\sum_{node=1}^{6} wmip3(node) = \\ &= \sum_{i3=1}^{n3}\sum_{ip3=1}^{nip3}(wr+(1-wr))*(\alpha+\beta+\gamma)*mip3 = \\ &= \sum_{i3=1}^{n3}\sum_{ip3=1}^{nip3} mip3 = \sum_{ip=1}^{np} mip\end{aligned} \tag{46}$$

where $n$ is a number, $c$ the interpolation cell, $p$ a tracer, $i$ counting index, *3* triangular cell, $w$ weighted, $m$ mass, *node* the counting index for the nodes at the boundaries of a triangular cell, $wr$ the radial weighting factor of a tracer; $\alpha, \beta, \gamma$ are the barycentric coordinates from the three corner points of the basis of a triangular cell, so that $\alpha + \beta + \gamma = 1$.

Diminution of tracer mass can be observed in the spreading zones which is not induced by density differences. In other areas, a compaction of tracer mass is to be expected:

$$wMc \neq \sum_{ip=1}^{npc} wmipc \tag{47}$$

The tracer mass ratio, $Gmc$, of the cells deviates from the obligated value *1*:

$$Gmc = \left(\sum_{ip=1}^{npc} wmipc\right) / wMc \neq 1 \tag{48}$$

This formula describes a distortion of the tracer representation.

A *local tracer mass refresh* has been introduced to reduce this discrepancy of Eq.(48). At least, a deviation

$$dGmcmax = max.permissible|Gmc - 1| \tag{49}$$

is allowed. If

$$(Gmc - 1) > dGmcmax \tag{50}$$

applies in a cell, $c$, then distribute tracer mass of $c$ to the neighboring cells in such a way that

$$(Gmc - 1) = dGmcmax \tag{51}$$

The tracer mass

$$dwMc = \sum_{ip=1}^{npc} wmipc - wMc * (1 + dGmcmax) \tag{52}$$

has to be distributed to those neighboring cells, $cn$, that have a common edge with the cell, $c$, at least and that fulfill the condition

$$dwMcn = \sum_{ip=1}^{npcn} wmipcn - wMcn * (1 + dGmcmax) < 0 \tag{53}$$

If the neighboring cells, $cn$, have the capacity to hold the excess tracer mass of $c$, i.e., if

$$dwMc < -\left(\sum_{cn=1}^{ncn} dwMcn\right) \tag{54}$$

then $dwMc$ is to be distributed to the $cn$. The proportionality of the different tracer types is ensured. If

$$(1 - Gmc) > dGmcmax \tag{55}$$

applies in $c$ then remove tracer mass from $cn$ in an analogous way so that

$$(1 - Gmc) = dGmcmax. \tag{56}$$

## 4 Results and Discussion of the Figures

### 4.1 Thermal and Chemical Evolution Using a Reference Run

We begin by presenting what we call our reference run 808B. It is representative of the results we obtain in a moderately extensive region of Rayleigh number – yield stress parameter space. Our chosen reference run is defined by a viscoplastic yield stress $\sigma_y = 115$ MPa and a viscosity-level parameter $r_n = -0.65$. Run 808B starts with eight tracers per grid-point cell. Now, we present the Figures, in each case immediately followed by the corresponding discussion. In Figure 1, the laterally averaged temperature for the geological present time as a function of depth is represented by a solid line. This curve lies

closer to the geotherm of a parameterized whole-mantle convection model than to the corresponding layered-convection temperature. This is understandable since the results of the present model, S3, show whole-mantle convection. However, the flow is somewhat impeded by the high-viscosity transition zone and by the endothermic 660-km phase boundary. Therefore, the temperature is slightly augmented, especially immediately beneath the 660-km boundary.

Figure 2 displays the laterally averaged present-day viscosity. Its derivation and discussion is given by Section 3.2. Figure 3 shows the time dependence of some spatially integrated quantities in our reference run. The evolution of the laterally averaged heat flow at the Earth's surface is depicted in the first panel. The curve reaches a realistic value for the present time: The observed mean global heat flow has been estimated to be 87 mW/m$^2$ (*Pollak et al.* [83]). The second panel exhibits the growth rate of continental mass as a function of time. It mimics observational indications that global magmatism and orogenesis are intrinsically episodic (*Worsley et al.* [119], *Nance et al.* [76], *Hoffman* [47], *Titley* [103], *Lister et al.* [69], *Condie* [28]). The third panel of Figure 3 demonstrates the time dependence of *Ror*, the ratio of surface heat outflow to the mantle's radiogenic heat production which is the

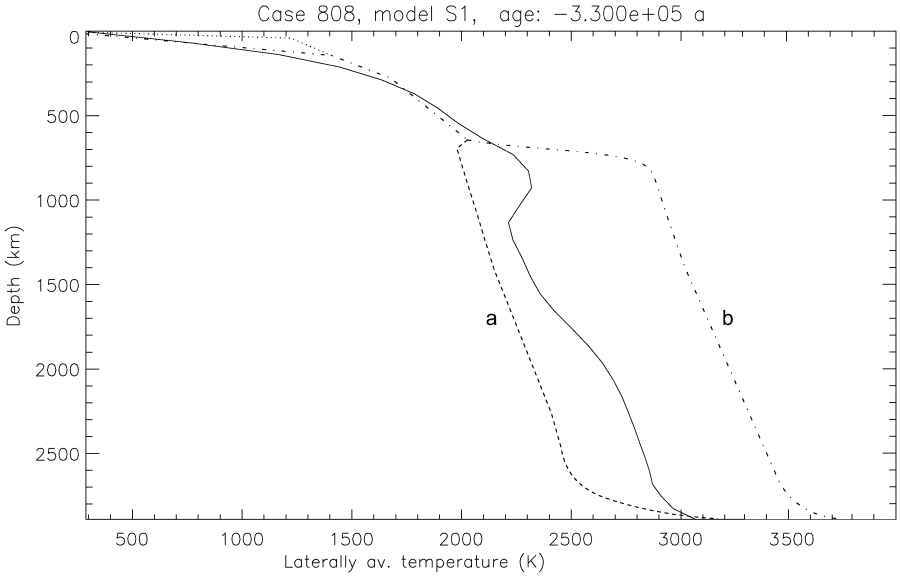


**Fig. 1.** The laterally averaged temperature of the geological present time (solid curve) as a function of depth for the reference run with a viscoplastic yield stress, $\sigma_y = 115$ MPa, and a viscosity level parameter, $r_n = -0.65$. Cf. Eqs. (33) and (34). A range of realistic mantle geotherms using parameterized models of the mantle's thermal history given by *Schubert et al.* [94] is depicted for comparison. Label a and b signify geotherms of whole-mantle and partially layered convection, respectively. The dotted line denotes a mid-oceanic ridge geotherm.

reciprocal value of the Urey number. Parameterized models show roughly similar curves except for medium-large and smaller fluctuations. A pattern of general decrease and some fluctuations in the Rayleigh number are indicated in the fourth panel.

The chemical heterogeneity of incompatible elements in a run with 64 tracers per grid-point cell for present time is shown by Figure 4. It is remarkable that in spite of 4500 Ma of solid-state mantle convection chemical reservoirs continue to persist. This paper therefore represents a possible way to reconcile the geochemical and geophysical constraints. Heterogeneities are diminished only by stirring (*Gottschaldt et al.* [38]). Diffuse mixing is negligible. However, in our model there are no pure unblended reservoirs, and this may also be true of the Earth's mantle. DMM predominates immediately below the continents (red) and beneath the oceanic lithosphere. This is a realistic feature of the model since where the real oceanic lithosphere is rifted, MORB magma is formed by decompression melting. The MORB source (DMM) is not only depleted in incompatible elements but also relatively homogenized. It is homogenized not only with respect to its major geochemical components ($SiO_2$, MgO, FeO, $Al_2O_3$, CaO) (*Palme and O'Neill* [80]) but also with respect to isotope ratios $^{87}Sr/^{86}Sr$, $^{143}Nd/^{144}Nd$, $^{206}Pb/^{204}Pb$, $^{207}Pb/^{204}Pb$ and $^{208}Pb/^{204}Pb$. As a consequence, the standard deviation of these isotope ratios and of the major element compositions is small for MORBs in comparison to OIBs (*Allègre and Levin* [4]) although *Hofmann* [50] has modified this conclusion somewhat. Figure 4 shows a marble-cake mantle as it was suggested by *Coltice and Ricard* [27] and *Becker et al.* [9] but reversed in terms of its pattern. It is the *depleted* regions in our model that are disconnected and

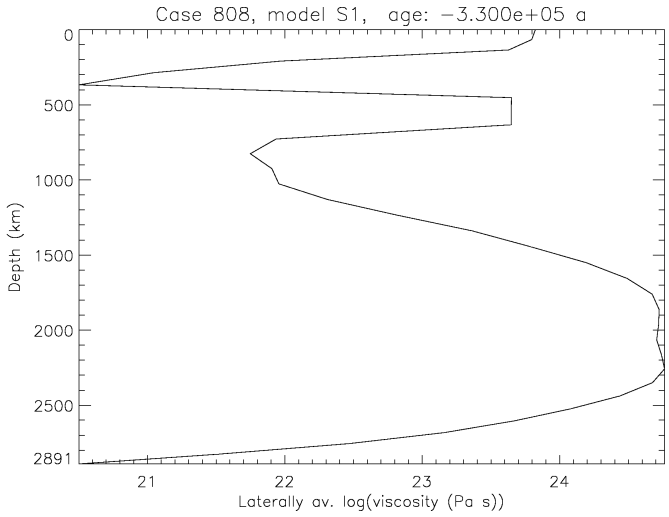


**Fig. 2.** The laterally averaged shear viscosity of the reference run as a function of depth for the present geological time.

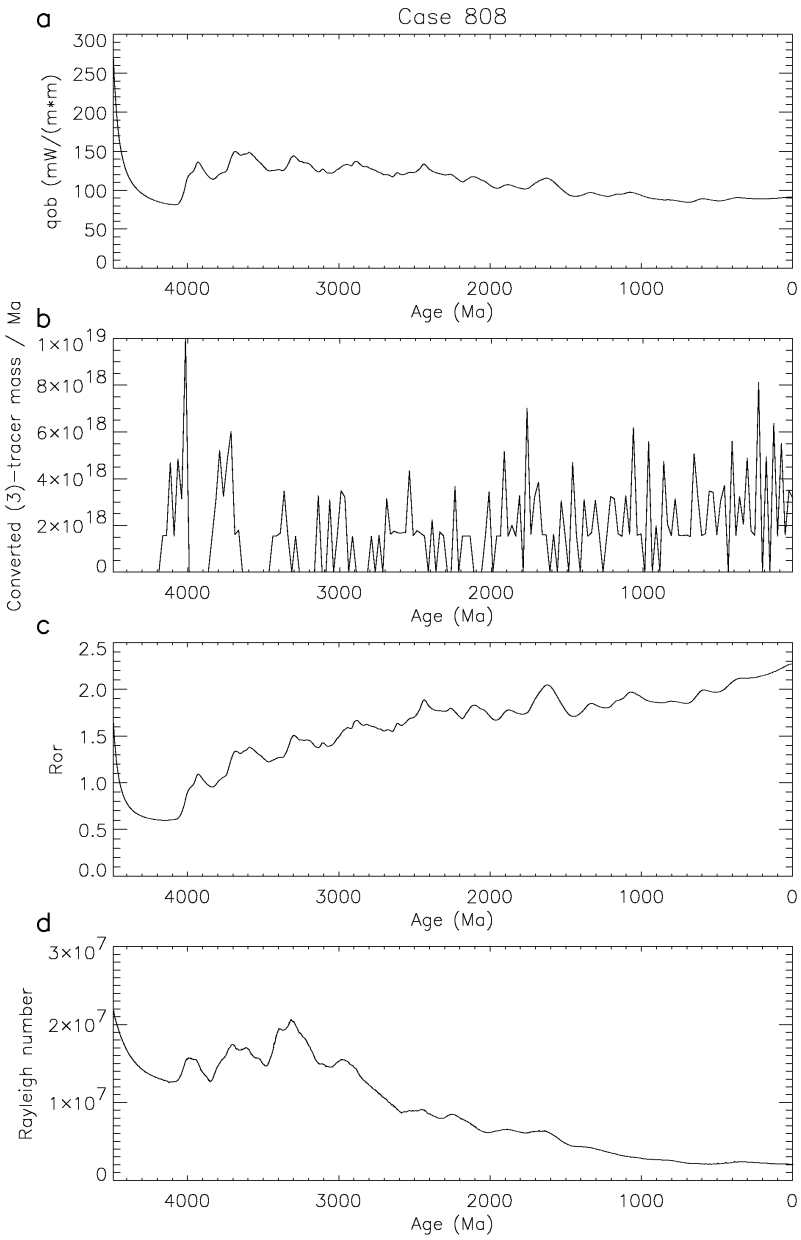


**Fig. 3.** Time evolution of some spatially integrated quantities from the reference run. **(a)** The laterally averaged surface heat flow, *qob*. **(b)** The juvenile contributions to the total mass of the continents. The genuine increase of continental material is expressed as converted Type-3 tracer mass per Ma. **(c)** The reciprocal value of the Urey number. *Ror* represents the *r*atio of the surface heat *o*utflow to the mantle's *r*adiogenic heat production rate. **(d)** The Rayleigh number as a function of age.

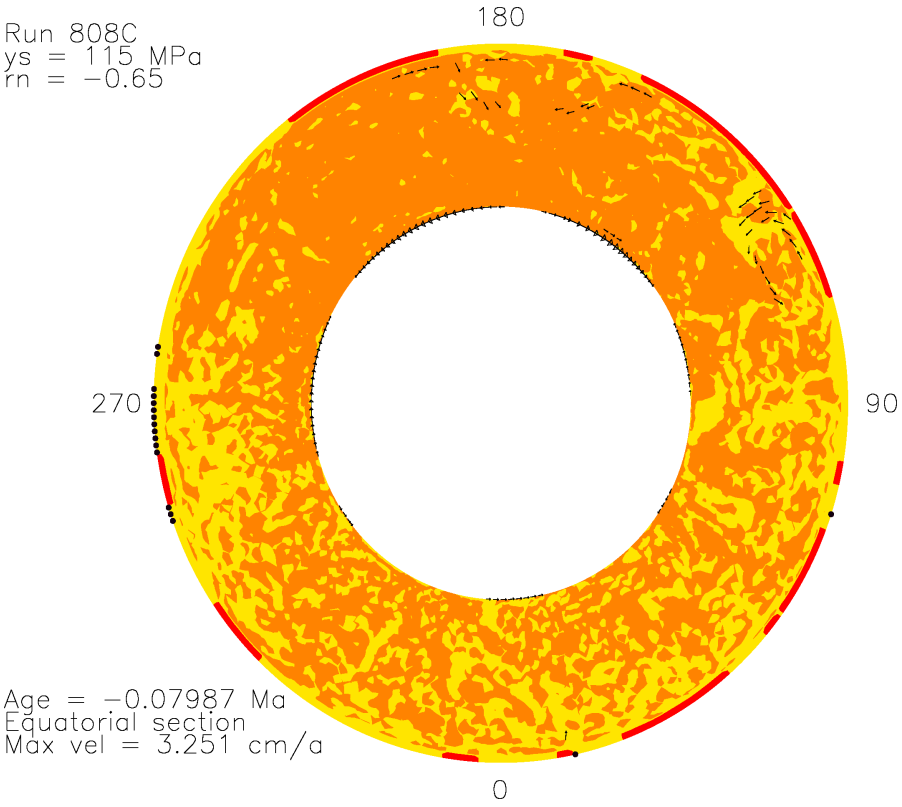


**Fig. 4.** This equatorial section shows the present-time state of the chemical evolution of the Earth's mantle as computed in a companion run, 808C, of run 808. Run 808C has 64 tracers per grid-point cell at the beginning. Strongly depleted parts of the mantle which include more than 50 % of depleted MORB mantle are represented by yellow areas. Less depleted and rich parts of the mantle are depicted by orange colors. Rich refers to a high abundance of incompatible elements. Continents are signified in red. Black dots stand for oceanic plateaus.

distributed like raisins. Furthermore the present model, S3, does not present difficulties with the buoyancy since the present chemical differences refer to the incompatible elements and not to the geochemical major components. It is remarkable that we did not obtain simply connected volumes for any geochemical reservoir. Nevertheless, the depleted volumes tend to be in the upper parts of the mantle. This is not amazing since chemical differentiation takes place just beneath the lithosphere and the low viscosity of the asthenosphere promotes mixing and lateral migration of DMM.

Figure 5 shows the present-time distribution of continents (red) of our reference run. The oceanic plateaus (black dots) are carried along by the self-consistently generated, moving oceanic lithosphere. If the plateaus touch a

continent they join with it. This is the only additional implementation. Neither number nor form nor size of the continents is prescribed. The configuration results simply from the numerical solution of the system of equations and the initial and boundary conditions. At first, the comparison with the observed present-day continents was carried out simply visually. Then we decided to represent both topographies, the observed one and the theoretical one, in terms of spherical harmonics

$$\{A_n^m \quad or \quad B_n^m\} = \pi^{-1} \cdot (2n+1)^{1/2} \cdot 2^{-1/2} \cdot [(n-m)!]^{1/2} \cdot [(n+m)!]^{-1/2} \cdot$$
$$\cdot \int_0^{2\pi} \{\cos m\phi \quad or \quad \sin m\phi\} \cdot \left[ \int_0^{\pi} f(\theta,\phi) \cdot P_{n,m}(\cos\theta) \cdot \sin\theta \cdot d\theta \right] d\phi, \qquad (57)$$

respectively, where $f(\theta,\phi)$ is topographic height. While the individual coefficients $A_n^m$ or $B_n^m$ depend on the position of the pole of the grid $(\theta,\phi)$, the quantity $h_n^*$ is orientation-independent:

$$h_n^* = n^{1/2} \cdot (n+1)^{1/2} \cdot 2^{-1} \cdot \left\{ \sum_{m=0}^{n} \left( (A_n^m)^2 + (B_n^m)^2 \right] \right\}^{1/2} \qquad (58)$$

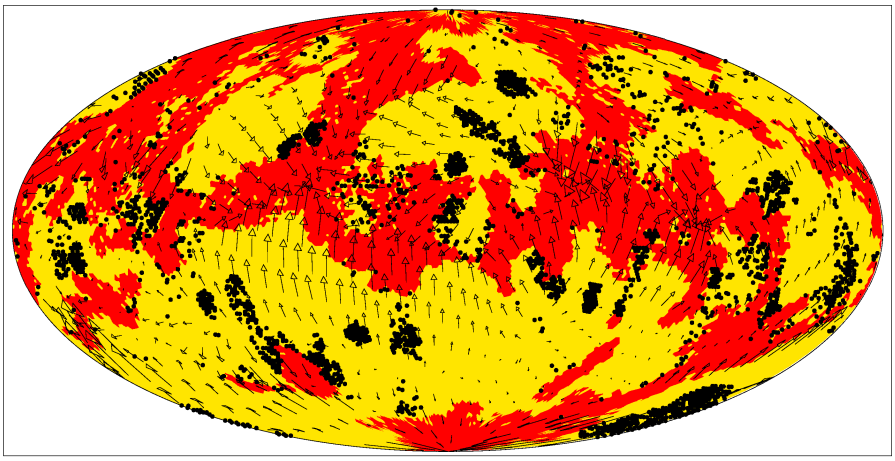


**Fig. 5.** The distribution of red continents and black oceanic plateaus at the Earth's surface for the geological present time according to the reference run with yield stress $\sigma_y = 115$ MPa and viscosity-level parameter $r_n = -0.65$. Arrows denote velocity. The oceanic lithosphere is denoted in yellow. There are no prescriptions concerning number, size or form of continents in the present model.

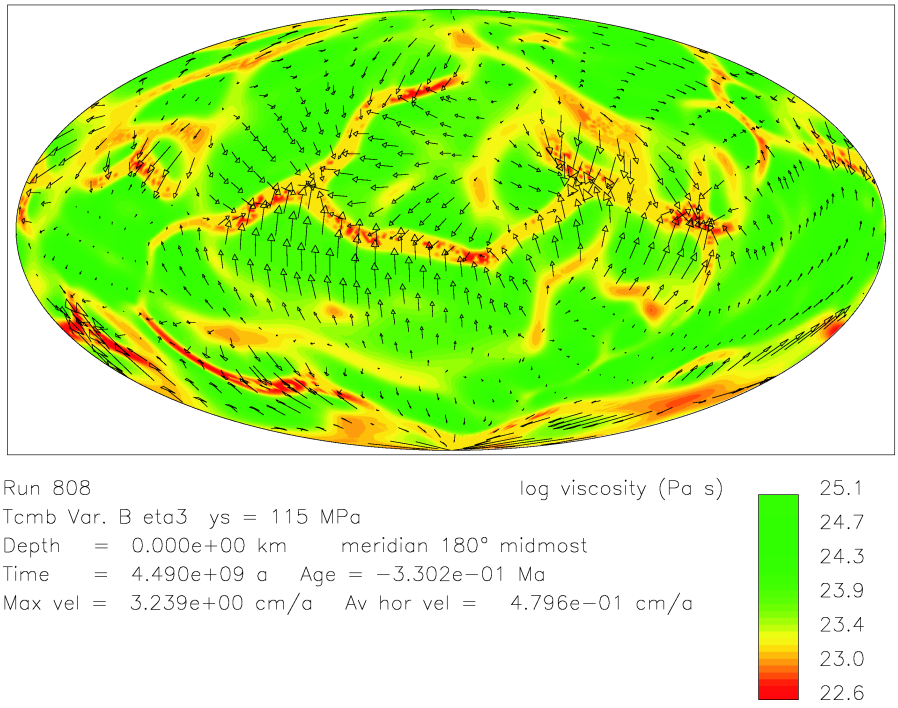


**Fig. 6.** The surface distribution of log viscosity (Pa·s) on an equal-area projection for the geological present time for the reference run. The velocity field displays plate-like character. Elongated high strain-rate zones lead to reduced viscosity because of viscoplastic yielding.

We are not aware of other papers on spherical-shell mantle convection with continents that evolve due to physical laws and that are *not* simply put onto the surface.

Figure 6 reveals the plate-like motions of the lithospheric patches at the surface. This kind of motion arises because of the viscosity law that includes yield stress. It has nothing to do with the tracers. It arises in similar models without tracers. The colors represent the logarithm of the viscosity in Pa·s. Figure 7 exhibits the present-time temperature on an equal-area projection of a spherical surface at 134.8 km depth. The blue zones corresponding to cold, subducting rock correlate with convergent zones at the surface.

### 4.2 Variation of Parameters: The Evolution of Continents

We varied the parameters $Ra$ and $\sigma_y$ to investigate the region in which we obtain Earth-like results and to find other regions with different mechanisms. A multitude of runs were performed to convince us that the selected reference run is by no means exceptional but representative of a notable portion of the

parameter space. We find that the general character of our results does not deviate too far from that of the real Earth. We compare the number, size, form and distribution of the calculated continents with the continent configuration of the present Earth. Earth-like continent solutions are shown by little black disks in the center of the $Ra$-$\sigma_y$ plot of Figure 8. $Ra$ denotes the temporal average of the Rayleigh number of a given run. Figures 9 and 10 display present-time continent distributions from two other runs, with $\sigma_y = 130$ MPa and $\sigma_y = 115$ MPa, respectively, and for $r_n = -0.6$ in both cases. We performed further studies to attempt to refine the Earth-like $Ra$-$\sigma_y$ area. Figure 11 describes a quantitative measure of the deviation of the calculated present-time continental area from the observed one. Favorable agreement occurs in the center of the $Ra$-$\sigma_y$ area. Favorable means that Earth-like solutions can be found in both Figures 8 *and* 11 in the *common* part of the $Ra$-$\sigma_y$ field.

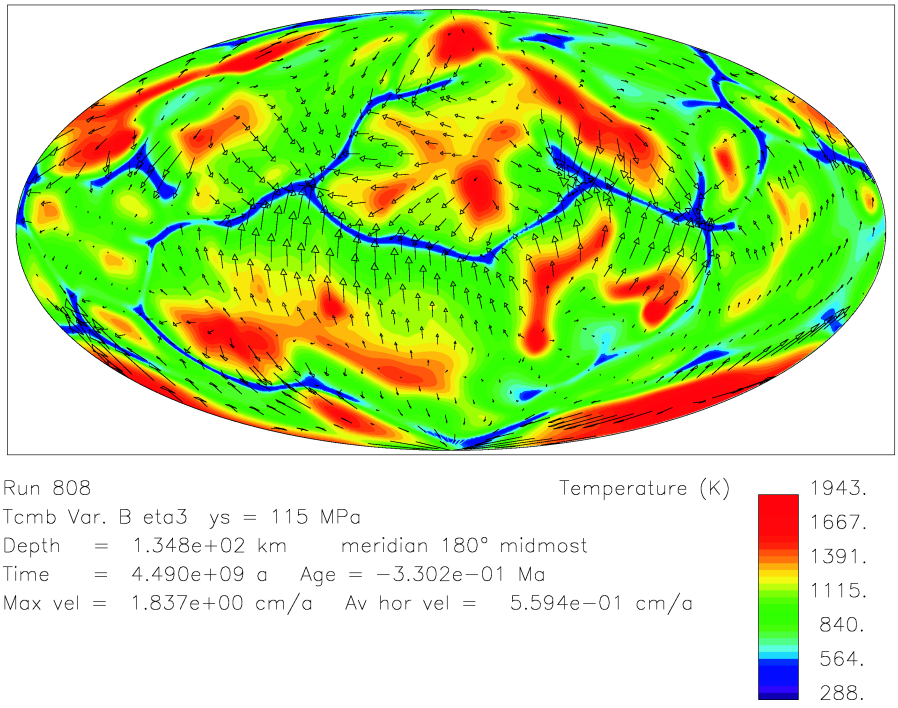


**Fig. 7.** Equal-area projection with the temperature distribution (colors) and the velocities (arrows) for the geological present for the reference run at a depth of 134.8 km. The narrow blue sheet-like subducting zones are evident also at greater depths. The slab-like features are narrow in comparison with the much broader upwellings.

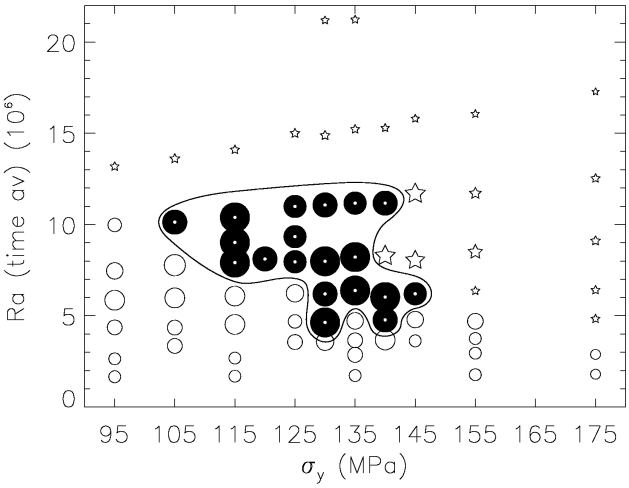


**Fig. 8.** The types of continental distribution as a function of yield stress, $\sigma_y$, and of temporally averaged Rayleigh number, $Ra$. Each symbol of the plot denotes one run. Little black disks with a white center signify Earth-like distributions of the continents where the size of the disk is a measure of quality. Five-pointed stars stand for distributions with an unrealistic multitude of tiny continents. White circles represent runs with reticularly connected, narrow stripe-like continents.

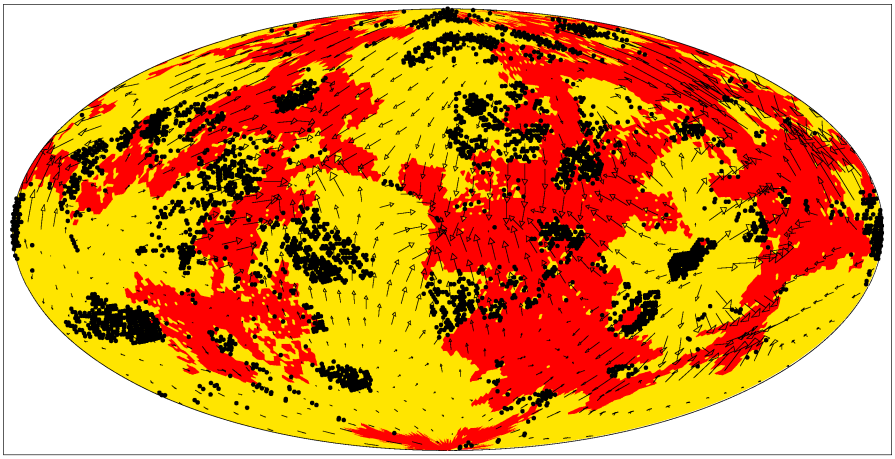

Run 797B ys = 130 MPa rn = −0.6 meridian 180° midmost
Time = 4.490e+09 a Age = −4.214e−01 Ma
Max vel = 1.609e+00 cm/a Av hor vel = 5.174e−01 cm/a

**Fig. 9.** Equal-area projection with the distribution of continents (red) and oceanic plateaus (black dots) for the geological present of a run with yield stress $\sigma_y = 130$ MPa and viscosity-level parameter $r_n = -0.6$. Yellow color stands for the oceanic lithosphere.

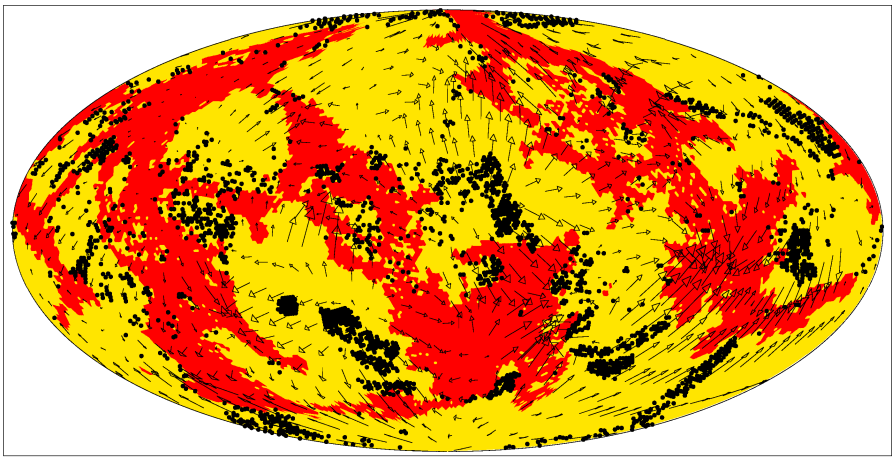


**Fig. 10.** The distribution of continents (red) and oceanic plateaus (black dots) for the geological present of a run with yield stress $\sigma_y = 115$ MPa and viscosity-level parameter $r_n = -0.6$. The oceanic lithosphere is signified by yellow color.

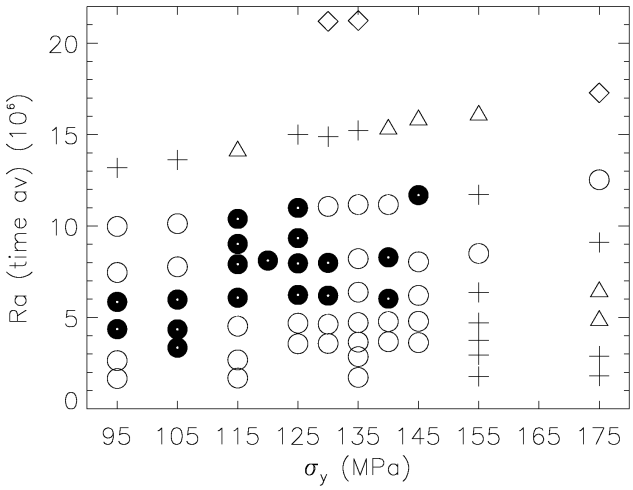


**Fig. 11.** A classification of the runs with respect to the difference of observed surface percentage of continents (=40.35%) minus calculated surface percentage of continents. This difference, $d_c$, is plotted as a function of yield stress, $\sigma_y$, and of the time average of the Rayleigh number, $Ra$. Little black disks denote slight deviations, namely $-4.5 \leq d_c < 4.5$ percent. White circles stand for $4.5 \leq d_c < 13.5$. Plus signs signify $13.5 \leq d_c < 22.5$. White triangles represent runs with $22.5 \leq d_c < 31.5$. White diamonds denote $31.5 \leq d_c < 40.5$.

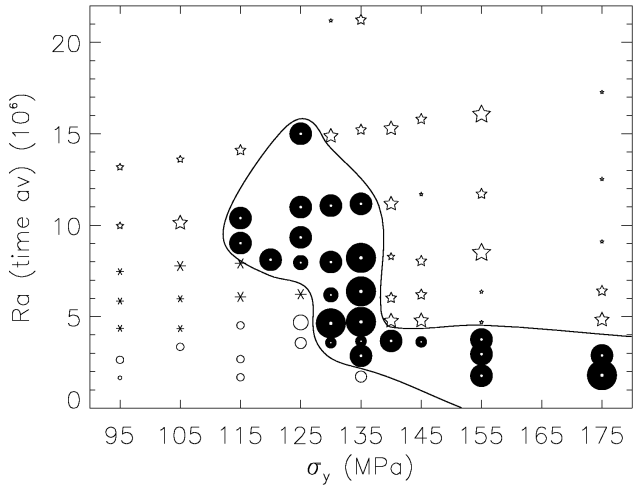


**Fig. 12.** The types of lithospheric movements as a function of yield stress, $\sigma_y$, and time average of the Rayleigh number, *Ra*. *Plate-like solutions* with narrow subducting zones are depicted by little black disks. Its surface area is a measure of plateness. White circles represent runs with broad downwellings and minor plateness. White five-pointed stars denote unrealistic runs with local subduction only. Asterisks stand for rather complex planforms with lots of small but not narrow downwellings.

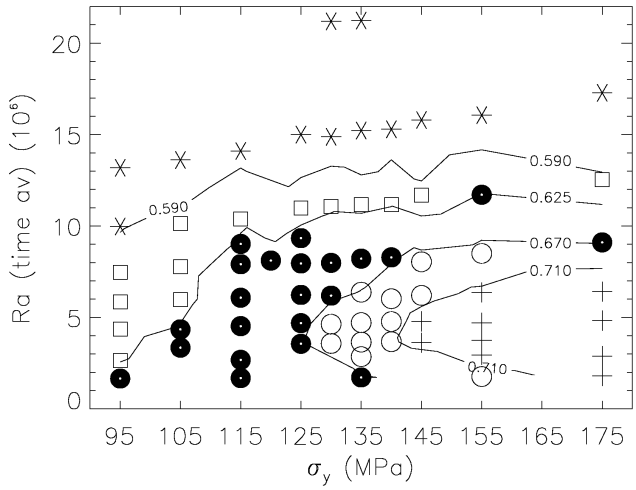


**Fig. 13.** The time average of the Urey number, $Ur$ is plotted in a diagram the abscissa of which is the yield stress, $\sigma_y$, and the ordinate is the time average of the Rayleigh number, *Ra*. Asterisks represent runs with $Ur \leq 0.59$. White squares stand for $0.59 < Ur \leq 0.625$. Little black disks denote runs with $0.625 < Ur \leq 0.67$. White circles depict runs with $0.67 < Ur \leq 0.71$. Finally, plus signs signify runs with $0.71 < Ur$.

### 4.3 Variation of Parameters: Plateness of Oceanic Lithospheric Pieces and Other Features

A classification of runs in terms of the planforms of flow near the surface is presented by Figure 12. Black disks denote plate-like solutions. An overlap set of the black disks is observed with the black disks of Figures 8 and 11. Figure 13 shows the distribution of classes of Urey numbers as a function of yield stress, $\sigma_y$, and time average of the Rayleigh number, $Ra$. Runs with realistic Urey numbers are pictured by black disks. For a comparison of the present-time laterally averaged heat flows, $qob(now)$, of the runs, it is important to filter away the random fluctuations. A simple method to do so is to replace the calculated values of $qob(now)$ by $qob^*$ where

$$qob^* = mean[qob(now)/qob(time\ av)] * qob(time\ av) \tag{59}$$

The expression *time av* denotes the time average of one run, *mean* stands for the average of all runs of the plot. Figure 14 demonstrates the distribution of the filtered present-time surface average of the heat flow, $qob^*$, in an $r_n - \sigma_y$ diagram. Realistic values are again denoted by black disks. A partial covering with the favorable field of continent distribution of Figure 5 is established.

Figure 15 shows the present-time theoretical flow spectrum $n^{1/2} \times (n+1)^{1/2} \times \langle v^2_{n,pol} \rangle$ of the reference run (lower curve) in comparison with the spectra of the total observed topography, $T$, and of the observed sea-floor topography, $S$, of the global JGP95E Digital Elevation Model (*Lemoine*

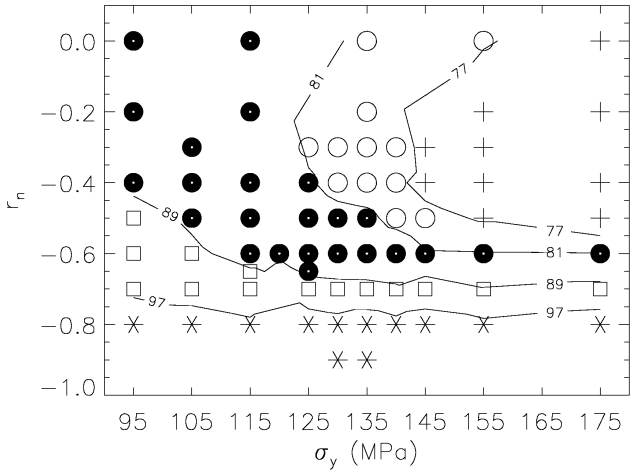


**Fig. 14.** The symbols represent classes of the non-random values, $qob^*$, of the present-time surface average of the heat flow of the runs in a $r_n$-$\sigma_y$ plot where $qob^*$ is calculated using Eq. (59). The following numbers are given in mW/m$^2$. Asterisks signify runs with $97 \leq qob^*$. White squares depict runs with $89 \leq qob^* < 97$, little black disks stand for $81 \leq qob^* < 89$. White circles denote runs with $77 \leq qob^* < 81$, plus signs represent the range $qob^* < 77$.

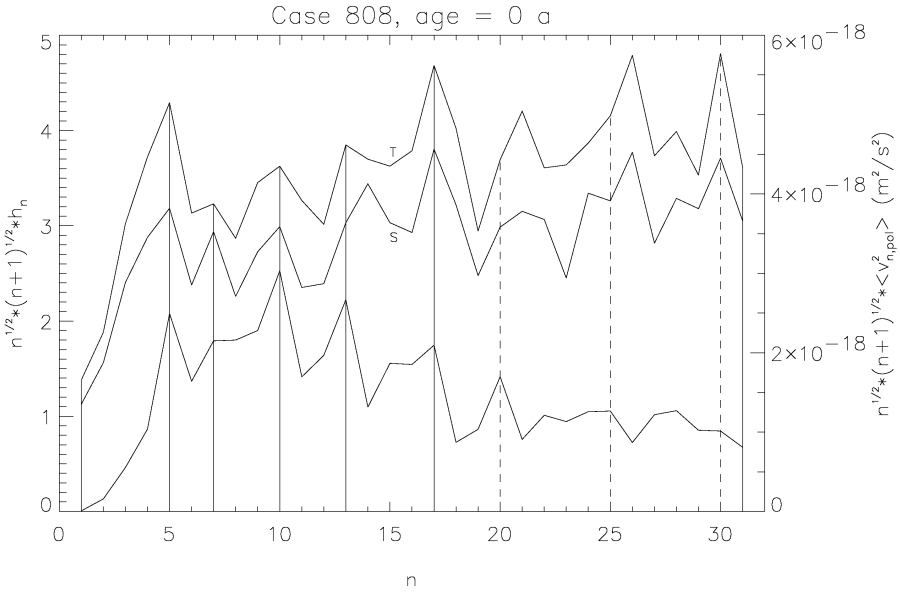


**Fig. 15.** A comparison of the orientation-independent quantities $h_n^*$ of the total flow of the Earth, $T$, and of the bathymetry, $S$, with the theoretical flow spectrum $n^{1/2}*(n+1)^{1/2}*\langle v_{n,pol}^2\rangle$ of the reference run (lower curve). The observational curves $T$ and $S$ have been calculated from the topography of the global JGP95E Digital Elevation Model of *Lemoine et al.* [67], chapter 2.

*et al.* [67]). It would be senseless to compare the different sets of coefficients $A_n^m$ and $B_n^m$ of Eq. (57) since they depend on the position of the pole of the coordinate system. The quantity $h_n^*$ of Eq. (58) is, however, independent on the orientation of the pole. The comparison of the theoretical spectrum $h_n^*(n)$ with that of $T$ shows a coincidence of the maxima up to n=17. A correspondence for higher values of $n$ is not to be expected because of the simplicity of the model. The perpendicular auxiliary lines are therefore only in five-unit distances for the higher-$n$ region.

## 5 Conclusions

The main subject of this paper is a combined segregation-convection theory in a 3-D compressible spherical-shell mantle. It is a step toward a reconciliation of seemingly contradictory geochemical and geophysical findings and a preliminary answer to three questions: (a) Did the differentiation of the mass of the continental crust (CC) take place predominantly at the beginning of the Earth's evolution similar to the cases of the Moon and Mars in which chemical segregation occured in the first 200 Ma, or have there been other modes of crustal production that continue to add juvenile crust in batches

possibly connected with episodic orogenesis? (b) How can different geochemical reservoirs be maintained in spite of persisting whole-mantle convection? (c) Why is DMM more homogeneous than other reservoirs?

Our modeling suggests the following simplified answers: (a) Similar to the cases of the Moon and Mars, part of the Earth's crust was probably also formed from a magma ocean, whether also CC was formed at this point is unknown. Nevertheless, since the mantle has been solid, our model indicates there have been episodes of CC growth comparable to magmatic and tectonic episodes in the Earth's history (cf. Figure 3, second panel). (b) The essential cause for the long-term conservation of complex mantle reservoirs less depleted than DMM is a high-viscosity zone in the central part of the lower mantle. Furthermore, the endothermal 660-km phase boundary and a possible high-viscosity transition layer also retard the stirring. (c) DMM is produced in the conventional asthenosphere and is distributed by convection also to other parts of the mantle. Since the asthenosphere has the lowest viscosity, the stirring is most effective there.

Moreover, the Figures 4,5,8,9,10,11 and 15 show that our model, S3, generates convincing present-time distributions of continents. Although the problem of oceanic lithospheric plate generation is not the focus of this paper as in *Trompert and Hansen* [108], *Tackley* [100, 101], *Richards et al.* [88], *Bercovici and Karato* [11], *Walzer et al.* [113] and *Bercovici and Ricard* [13], we want to remark that also S3 shows good plate-like solutions (cf. Figure 12). Other conclusions that we do not want to repeat here can be found in the Abstract.

## Acknowledgements

We gratefully acknowledge the help of Dave Stegman. He provided us with his particle code and discussed some problems with us. This work was partly supported by the Deutsche Forschungsgemeinschaft under grant WA 1035/5-3. We kindly acknowledge the use of supercomputing facilities at HLRS Stuttgart and NIC Jülich. The major part of the simulations was performed on the Cray Strider Opteron cluster at the High Performance Computing Center (HLRS) under the grant number *sphshell* /12714.

## References

1. O. Alard, W.L. Griffin, J.P. Lorand, S.E. Jackson, and S.Y. O'Reilly. Non-chondritic distribution of the highly siderophile elements in mantle sulphides. *Nature*, 407:891–894, 2000.
2. F. Albarède and R. van der Hilst. Zoned mantle convection. *Philosophical Transactions of the Royal Society A: Mathematical, Physical and Engineering Sciences*, 360:2569–2592, 2002.

3. C.J. Allègre. The evolution of mantle mixing. *Philosophical Transactions of the Royal Society A: Mathematical, Physical and Engineering Sciences*, 360:2411–2431, 2002.
4. C.J. Allègre and E. Levin. Isotopic systems and stirring times of the Earth's mantle. *Earth and Planetary Science Letters*, 136:629–646, 1995.
5. Y. Amelin, D.C. Lee, and A.N. Halliday. Early-middle Archean crustal evolution from Lu-Hf and U-Pb isotopic studies of single zircon grains. *Geochimica et Cosmochimica Acta*, 64:4205–4225, 2000.
6. R.L. Armstrong. The persistent myth of crustal growth. *Austral. J. Earth Sci.*, 38:613–640, 1991.
7. N. Arndt. Crustal growth rates. In K. Eriksson, W. Altermann, D.R. Nelson, W.U. Mueller, and O. Catuneanu, editors, *The Precambrian Earth: Tempos and Events (Developments in Precambrian Geology, Vol. 12)*, pages 155–157. Elsevier, Amsterdam, 2004.
8. D.N. Barfod, C.J. Ballentine, A.N. Halliday, and J.G. Fitton. Noble gases in the Cameroon line and the He, Ne, and Ar isotopic compositions of HIMU mantle. *Journal of Geophysical Research*, 104:29509–29527, 1999.
9. T.W. Becker, J.B. Kellogg, and R.J. O'Connell. Thermal constraints on the survival of primitive blobs in the lower mantle. *Earth and Planetary Science Letters*, 171:351–365, 1999.
10. V.C. Bennett. Compositional evolution of the mantle. In R.W. Carlson, editor, *Treatise on Geochemistry, Vol.2: The Mantle and the Core*, pages 493–519. Elsevier, Amsterdam, 2003.
11. D. Bercovici and S. Karato. Theoretical analysis of shear localisation in the lithosphere. In S. Karato and H. Wenk, editors, *Plastic Deformation of Minerals and Rocks (Rev. Mineral. Geochem.)*, volume 51, pages 387–420. Mineral. Soc. of Am., Washington, D.C., 2002.
12. D. Bercovici and S.-I. Karato. Whole-mantle convection and the transition-zone water filter. *Nature*, 425:39–44, 2003.
13. D. Bercovici and Y. Ricard. Tectonic plate generation and two-phase damage: Void growth versus grain size reduction. *Journal of Geophysical Research*, 110:B03401, 2005.
14. C.R. Bina. Seismological constraints upon mantle composition. In R.W. Carlson, editor, *Treatise on Geochemistry, Vol.2: The Mantle and the Core*, pages 39–59. Elsevier, Amsterdam, 2003.
15. D.D. Bogard, R.N. Clayton, K. Marti, T. Owen, and G. Turner. Chronology and evolution of Mars. *Space Sci. Rev.*, 96:425–458, 2001.
16. S.A. Bowring and T. Housh. The Earth's early evolution. *Science*, 269:1535–1540, 1995.
17. A.D. Brandon, R.J. Walker, J.W. Morgan, and G.G. Goles. Re-Os isotopic evidence for early differentiation of the Martian mantle. *Geochimica et Cosmochimica Acta*, 64:4083–4095, 2000.
18. B.A. Buffett, H.E. Huppert, J.R. Lister, and A.W. Woods. On the thermal evolution of the Earth's core. *Journal of Geophysical Research*, 101:7989–8006, 1996.
19. H.-P. Bunge. *Global mantle convection models*. PhD thesis, UC Berkeley, 1996.
20. H.-P. Bunge and J.R. Baumgardner. Mantle convection modelling on parallel virtual machines. *Computers in Physics*, 9:207–215, 1995.

21. H.-P. Bunge, M.A. Richards, and J.R. Baumgardner. A sensitivity study of three-dimensional spherical mantle convection at $10^8$ Rayleigh number: Effects of depth-dependent viscosity, heating mode and an endothermic phase change. *Journal of Geophysical Research*, 102:11991–12007, 1997.
22. K.W. Burton, P. Schiano, J.-L. Birck, C.J. Allègre, M. Rehkämper, A.N. Halliday, and J.B. Dawson. The distribution and behavior of rhenium and osmium amongst mantle minerals and the age of the lithospheric mantle beneath Tanzania. *Earth and Planetary Science Letters*, 183:93–106, 2000.
23. A.G.W. Cameron. The first ten million years in the solar nebula. *Meteoritics*, 30:133–161, 1995.
24. U.R. Christensen and D.A. Yuen. Layered convection induced by phase transitions. *Journal of Geophysical Research*, 90:10291–10300, 1985.
25. M.F. Coffin and O. Eldholm. Large igneous provinces: Crustal structure, dimensions and external consequences. *Reviews of Geophysics*, 32:1–36, 1994.
26. N. Coltice and Y. Ricard. Geochemical observations and one layer mantle convection. *Earth and Planetary Science Letters*, 174:125–137, 1999.
27. N. Coltice and Y. Ricard. On the origin of noble gases in mantle plumes. *Philosophical Transactions of the Royal Society A: Mathematical, Physical and Engineering Sciences*, 360:2633–2648, 2002.
28. K.C. Condie. Incompatible element ratio in oceanic basalts and komatiites: tracking deep mantle sources and continental growth rates with time. *Geochemistry, Geophysics, Geosystems*, 4:1005, 1 2003.
29. V. Courtillot, A. Davaille, J. Besse, and J. Stock. Three distinct types of hot spots into the Earth's mantle. *Earth and Planetary Science Letters*, 205:295–308, 2003.
30. L. Cserepes, D.A. Yuen, and B.A. Schroeder. Effect of the mid-mantle viscosity and phase-transition structure on 3D mantle convection. *Physics of the Earth and Planetary Interiors*, 118:135–148, 2000.
31. G.F. Davies. Geophysical and isotopic constraints on mantle convection: An interim synthesis. *Journal of Geophysical Research*, 89:6017–6040, 1984.
32. A.M. Dziewonski and D.L. Anderson. Preliminary reference Earth model. *Physics of the Earth and Planetary Interiors*, 25:297–356, 1981.
33. K.A. Farley, J.H. Natland, and H. Craig. Binary mixing of enriched and undegassed (primitive?) mantle components (He, Sr, Nd, Pb) in Samoan lavas. *Earth and Planetary Science Letters*, 111:183–199, 1992.
34. G. Fitton, J. Mahoney, P. Wallace, and A. Saunders, editors. *Origin and Evolution of the Ontong Java Plateau*, volume 229 of *GSL Special Publications*. Geological Society, London, 2004.
35. A.M. Forte and J.X. Mitrovica. Deep-mantle high-viscosity flow and thermochemical structure inferred from seismic and geodynamic data. *Nature*, 410:1049–1056, 2001.
36. J.J. Gilvarry. The Lindemann and Grüneisen laws. *Phys. Rev.*, 102:307–316, 1956.
37. G.A. Glatzmaier. Numerical simulations of mantle convection: Time-dependent, three-dimensional, compressible, spherical shell. *Geophys. Astrophys. Fluid Dyn.*, 43:223–264, 1988.
38. K.-D. Gottschaldt, U. Walzer, R.F. Hendel, D.R. Stegman, J.R. Baumgardner, and H.-B. Mühlhaus. Stirring in 3-d spherical models of convection in the Earth's mantle. *Philosophical Magazine*, 86:3175–3204, 2006.

39. S.P. Grand, R.D. van der Hilst, and S. Widiyantoro. Global seismic tomography: A snapshot of convection in the Earth. *GSA Today*, 7:1–7, 1997.
40. M. Gurnis. The effects of chemical density differences on convective mixing in the Earth's mantle. *Journal of Geophysical Research*, 91:11407–11419, 1986.
41. B.B. Hanan and D.W. Graham. Lead and helium isotope evidence from oceanic basalts for a common deep source of mantle plumes. *Science*, 272:991–995, 1996.
42. S.R. Hart, E.H. Hauri, L.A. Oschmann, and J.A. Whitehead. Mantle plumes and entrainment: Isotopic evidence. *Science*, 256:517–520, 1992.
43. K.S. Heier. The distribution and redistribution of heat-producing elements in the continents. *Philosophical Transactions of the Royal Society A: Mathematical, Physical and Engineering Sciences*, 288:393–400, 1978.
44. G.R. Helffrich and B.J. Wood. The Earth's mantle. *Nature*, 412:501–507, 2001.
45. D.R. Hilton and D. Porcelli. Noble gases as mantle tracers. In R.W. Carlson, editor, *Treatise on Geochemistry, Vol.2: The Mantle and the Core*, pages 277–318. Elsevier, Amsterdam, 2003.
46. K. Hirose. Phase transitions in pyrolitic mantle around 670-km depth: Implications for upwelling of plumes from the lower mantle. *Journal of Geophysical Research*, 107(B4):2078, 2002.
47. P.F. Hoffman. Speculations on Laurentia's first gigayear (2.0 to 1.0 Ga). *Geology*, 17:135–138, 1989.
48. A.W. Hofmann. Chemical differentiation of the Earth: The relationship between mantle, continental crust and oceanic crust. *Earth and Planetary Science Letters*, 90:297–314, 1988.
49. A.W. Hofmann. Mantle geochemistry: The message from oceanic volcanism. *Nature*, 385:219–229, 1997.
50. A.W. Hofmann. Sampling mantle heterogeneity through oceanic basalts: Isotopes and trace elements. In R.W. Carlson, editor, *Treatise on Geochemistry, Vol.2: The Mantle and the Core*, pages 61–101. Elsevier, Amsterdam, 2003.
51. A.W. Hofmann, K.-P. Jochum, M. Seufert, and W.M. White. Nb and Pb in oceanic basalts: New constraints on mantle evolution. *Earth and Planetary Science Letters*, 79:33–45, 1986.
52. S. Honda and Y. Iwase. Comparison of the dynamic and parameterized models of mantle convection including core cooling. *Earth and Planetary Science Letters*, 139:133–145, 1996.
53. F.G. Houtermans. Determination of the age of the Earth from the isotopic composition of meteoritic lead. *Nuovo Cimento*, 10:1623–1633, 1953.
54. B.L. Isacks and P.M. Molnar. Distribution of stresses in the descending lithosphere from a global survey of focal-mechanism solutions of mantle earthquakes. *Reviews of Geophysics and Space Physics*, 9:103–174, 1971.
55. I. Jackson and S.M. Rigden. Composition and temperature of the Earth's mantle: Seismological models interpreted through experimental studies of Earth materials. In I. Jackson, editor, *The Earth's Mantle. Composition, Structure and Evolution*, pages 405–460. Cambridge University Press, Cambridge, UK, 1998.
56. K.P. Jochum, A.W. Hofmann, E. Ito, H.M. Seufert, and W.M. White. K, U and Th in mid-ocean ridge basalt glasses and heat production, K/U and K/Rb in the mantle. *Nature*, 306:431–436, 1983.

57. S.-I. Karato. Phase transformations and rheological properties of mantle minerals. In D.J. Crossley, editor, *Earth's Deep Interior*, pages 223–272. Gordon and Breach Sci. Publ., 1997.
58. S.-I. Karato and P. Li. Diffusion creep in perovskite: implications for the rheology of the lower mantle. *Science*, 255:1238–1240, 1992.
59. S.-I. Karato, Z. Wang, B. Liu, and K. Fujino. Plastic deformation of garnets: systematics and implications for the rheology of the mantle transition zone. *Earth and Planetary Science Letters*, 130:13–30, 1995.
60. S.-I. Karato and P. Wu. Rheology of the upper mantle: a synthesis. *Science*, 260:771–778, 1993.
61. M. Kido and O. Čadek. Inferences of viscosity from the oceanic geoid: indication of a low viscosity zone below the 660-km discontinuity. *Earth and Planetary Science Letters*, 151:125–137, 1997.
62. M. Kido and D.A. Yuen. The role played by a low viscosity zone under a 660 km discontinuity in regional mantle layering. *Earth and Planetary Science Letters*, 181:573–583, 2000.
63. M. Kido, D.A. Yuen, O. Čadek, and T. Nakakuki. Mantle viscosity derived by genetic algorithm using oceanic geoid and seismic tomography for whole-mantle versus blocked-flow situations. *Physics of the Earth and Planetary Interiors*, 107:307–326, 1998.
64. S.H. Kirby, S. Stein, E.A. Okal, and D.C. Rubie. Metastable mantle phase transformations and deep earthquakes in subducting oceanic lithosphere. *Reviews of Geophysics*, 34:261–306, 1996.
65. T. Kleine, C. Muenker, K. Mezger, and H. Palme. Rapid accretion and early core formation on asteroids and the terrestrial planets from Hf-W chronometry. *Nature*, 418:952–955, 2002.
66. J.D. Kramers. Lead and strontium isotopes in Cretaceous kimberlites and mantle-derived xenoliths from Southern Africa. *Earth and Planetary Science Letters*, 34:419–431, 1977.
67. F.G. Lemoine, S.C. Kenyon, J.K. Factor, R.G. Trimmer, N.K. Pavlis, D.S. Chinn, C.M. Cox, S.M. Klosko, S.B. Luthcke, M.H. Torrence, Y.M. Wang, R.G. Williamson, E.C. Pavlis, R.H. Rapp, and T.R. Olson. The Development of the Joint NASA GSFC and the NIMA Geopotential Model EGM96. *NASA Goddard Space Flight Center*, NASA TP/-1998-206861:575 pp., 1998.
68. P. Li, S.-I. Karato, and Z. Wang. High-temperature creep in fine-grained polycristalline $CaTiO_3$, an analogue material of (Mg, Fe)$SiO_3$ perovskite. *Physics of the Earth and Planetary Interiors*, 95:19–36, 1996.
69. G.S. Lister, M.A. Forster, and T.J. Rawling. Episodicity during orogenesis. In J.A. Miller, R.E. Holdsworth, I.S. Buick, and M. Hand, editors, *Continental Reactivating and Reworking*, volume 184 of *GSL Special Publications*, pages 89–113. Geological Society, London, 2001.
70. C. Matyska and D.A. Yuen. Lower mantle dynamics with the post-perovskite phase change, radiative thermal conductivity, temperature- and depth-dependent viscosity. *Physics of the Earth and Planetary Interiors*, 154:196–207, 2006.
71. M.T. McCulloch and V.C. Bennett. Progressive growth of the Earth's continental crust and depleted mantle: Geochemical constraints. *Geochimica et Cosmochimica Acta*, 58:4717–4738, 1994.
72. M.T. McCulloch and V.C. Bennett. Early differentiation of the Earth: An isotopic perspective. In I. Jackson, editor, *The Earth's Mantle. Composition,*

*Structure and Evolution*, pages 127–158. Cambridge University Press, Cambridge, UK, 1998.
73. W.F. McDonough and S.-S. Sun. The composition of the Earth. *Chem. Geol.*, 120:223–253, 1995.
74. C. Meade and R. Jeanloz. The strength of mantle silicates at high pressures and room temperature: implications for the viscosity of the mantle. *Nature*, 348:533–535, 1990.
75. R. Montelli, G. Nolet, F.A. Dahlen, G. Masters, E.R. Engdahl, and S.-H. Hung. Finite-frequency tomography reveals a variety of plumes in the mantle. *Science*, 303:338–343, 2004.
76. R.D. Nance, T.R. Worsley, and J.B. Moody. Post-archean biogeochemical cycles and long-term episodicity in tectonic processes. *Geology*, 14:514–518, 1986.
77. M. Norman, L. Borg, L. Nyquist, and D. Bogard. Chonology, geochemistry and petrology of a ferroan noritic anorthosite clast from Descartes breccia 67215: clues to the age, origin, structure and impact history of the lunar crust. *Meteorit. Planet. Sci.*, 38:645–661, 2003.
78. L.E. Nyquist, D.D. Bogard, C.-Y. Shih, A. Greshake, D. Stöffler, and O. Eugster. Ages and geological histories of Martian meteorites. *Space Sci. Rev.*, 96:105–164, 2001.
79. R.K. O'Nions and I.N. Tolstikhin. Limits on the mass flux between lower and upper mantle and stability of layering. *Earth and Planetary Science Letters*, 139:213–222, 1996.
80. H. Palme and H.S.C. O'Neill. Cosmochemical estimates of mantle composition. In R.W. Carlson, editor, *Treatise on Geochemistry, Vol.2: The Mantle and the Core*, pages 1–38. Elsevier, Amsterdam, 2003.
81. S.V. Panasyuk and B.H. Hager. Inversion for mantle viscosity profiles constrained by dynamic topography and the geoid and their estimated errors. *Geophysical Journal International*, 143:821–836, 2000.
82. N.J. Pearson, O. Alard, W.L. Griffin, S.E. Jackson, and S.Y. O'Reilly. In situ measurement of Re-Os isotopes in mantle sulfides by laser ablation multicollector inductively coupled plasma mass spectrometry: analytical methods and preliminary results. *Geochimica et Cosmochimica Acta*, 66:1037–1050, 2002.
83. H.N. Pollak, S.J. Hurter, and J.R. Johnson. Heat flow from the Earth's interior: analysis of the global data set. *Reviews of Geophysics*, 31:267–280, 1993.
84. D. Porcelli and C.J. Ballentine. Models for the distribution of terrestrial noble gases and evolution of the atmosphere. In D. Porcelli, C.J. Ballentine, and R. Wieler, editors, *Noble Gases in Geochemistry and Cosmochemistry (Rev. Mineral. Geochem.)*, volume 47, pages 411–480. Mineral. Soc. of Am., Washington, D.C., 2002.
85. D. Porcelli and A.N. Halliday. The core as a possible source of mantle helium. *Earth and Planetary Science Letters*, 192:45–56, 2001.
86. A. Ramage and A.J. Wathen. Iterative solution techniques for finite element discretizations of fluid flow problems. In *Proceedings of the Copper Mountain Conference on Iterative Methods*, volume 1, Copper Mountain, Colorado, 1992.
87. A. Reymer and G. Schubert. Phanerozoic addition rates to the continental crust and crustal growth. *Tectonics*, 3:63–77, 1984.
88. M.A. Richards, W.-S. Yang, J.R. Baumgardner, and H.-P. Bunge. Role of a low-viscosity zone in stabilizing plate tectonics: Implications for comparative terrestrial planetology. *Geochemistry, Geophysics, Geosystems*, 3:1040, 2001.

89. F.M. Richter. Finite amplitude convection through a phase boundary. *Geophys. J. R. Astron. Soc.*, 35:265–276, 1973.
90. R.L. Rudnick and D.M. Fountain. Nature and composition of the continental crust: A lower crustal perspective. *Reviews of Geophysics*, 33:267–309, 1995.
91. R.L. Rudnick and S. Gao. Composition of the continental crust. In R.L. Rudnick, editor, *Treatise on Geochemistry, Vol.3: The Crust*, pages 1–64. Elsevier, Amsterdam, 2003.
92. V.J.M. Salters and W.M. White. Hf isotope constraints on mantle evolution. *Chem. Geol.*, 145:447–460, 1998.
93. H. Schmeling. A model of episodic melt extraction for plumes. *Journal of Geophysical Research*, 111:B03202, 2006.
94. G. Schubert, D.L. Turcotte, and T.R. Olson. *Mantle convection in the Earth and Planets*. Cambridge University Press, Cambridge, UK, 2001.
95. V. Steinbach and D.A. Yuen. Effects of depth-dependent properties on thermal anomalies produced in flush instabilities from phase transitions. *Physics of the Earth and Planetary Interiors*, 86:165–183, 1994.
96. V. Steinbach, D.A. Yuen, and W.L. Zhao. Instabilities from phase transitions and the timescales of mantle thermal convection. *Geophysical Research Letters*, 20:1119–1122, 1993.
97. D.J. Stevenson. Origin of the moon: the collision hypothesis. *Annu. Rev. Earth Sci.*, 15:271–315, 1987.
98. A. Stracke, A.W. Hofmann, and S.R. Hart. FOZO, HIMU and the rest of the mantle zoo. *Geochemistry, Geophysics, Geosystems*, 6:Q05007, 2005.
99. Y.J. Su. *Mid-ocean ridge basalt trace element systematics: Constraints from database management, ICP-MS analyses, global data compilation and petrologic modeling*. PhD thesis, Columbia University, 2002.
100. P. Tackley. The quest for self-consistent generation of plate tectonics in mantle convection models. In M.A. Richards, R. Gordon, and R. van der Hilst, editors, *History and Dynamics of Global Plate Motions, Geophysical Mograph Series, Vol. 121*, pages 47–72. American Geophysical Union, Washington, D.C., 2000.
101. P.J. Tackley. Self-consistent generation of tectonic plates in time-dependent, three-dimensional mantle convection simulations. *Geochemistry, Geophysics, Geosystems*, 1:No. 8, 2000.
102. S.R. Taylor and S.M. McLennon. *The Continental Crust: Its Composition and Evolution*. Blackwell Scientific, Oxford, 1985.
103. S.R. Titley. Relationship of stratabound ores with tectonic cycles of the phanerozoic and proterozoic. *Precambrian Research*, 61:295–322, 1993.
104. I. Tolstikhin and B. Marty. The evolution of terrestrial volatiles: A view from helium, neon, argon and nitrogen isotope modelling. *Chem. Geol.*, 147:27–52, 1998.
105. W.B. Tonks and H.J. Melosh. Magma ocean formation due to giant impacts. *Journal of Geophysical Research*, 98:5319–5333, 1993.
106. J. Trampert, F. Deschamps, J. Resovsky, and D.A. Yuen. Probabilistic tomography maps chemical heterogeneities throughout the lower mantle. *Science*, 306:853–856, 2004.
107. M. Trieloff and J. Kunz. Isotope systematics of noble gases in the Earth's mantle: Possible sources of primordial isotopes and implifications for mantle structure. *Physics of the Earth and Planetary Interiors*, 148:13–38, 2005.
108. R. Trompert and U. Hansen. Mantle convection simulations with rheologies that generate plate-like behavior. *Nature*, 395:686–689, 1998.

109. R. van der Hilst, S. Widiyantoro, and E.R. Engdahl. Evidence for deep mantle circulation from global tomography. *Nature*, 386:578–584, 1997.
110. P.E. van Keken, E.H. Hauri, and C.J. Ballentine. Mantle mixing: The generation, preservation and destruction of chemical heterogeneity. *Annu. Rev. Earth Planet Sci.*, 30:493–525, 2002.
111. J.D. Vervoort and J. Blichert-Toft. Evolution of the depleted mantle: Hf isotope evidence from juvenile rocks through time. *Geochimica et Cosmochimica Acta*, 63:533–556, 1999.
112. U. Walzer and R. Hendel. A new convection-fractionation model for the evolution of the principal geochemical reservoirs of the Earth's mantle. *Physics of the Earth and Planetary Interiors*, 112:211–256, 1999.
113. U. Walzer, R. Hendel, and J. Baumgardner. The effects of a variation of the radial viscosity profile on mantle evolution. *Tectonophysics*, 384:55–90, 2004.
114. U. Walzer, R. Hendel, and J. Baumgardner. Toward a thermochemical model of the evolution of the Earth's mantle. In E. Krause, W. Jäger, and M. Resch, editors, *High Performance Computing in Science and Engineering '04*, pages 395–454. Springer, Berlin, 2004.
115. K.H. Wedepohl. The composition of the continental crust. *Geochimica et Cosmochimica Acta*, 59:1217–1232, 1995.
116. M. Willbold and A. Stracke. Trace element composition of mantle endmembers: Implications for recycling of oceanic and upper and lower continental crust. *Geochemistry, Geophysics, Geosystems*, 7:Q04004, 2006.
117. M. Wilson and E.A. Spencer. The origin and evolution of the FOZO/PREMA and HIMU mantle components - the carbonatite perspective. http://www.geo.uw.edu.pl/ERASMUS/files/wilson3.ppt, 2003.
118. G. Wörner, A. Zindler, H. Staudigel, and H.U. Schmincke. Sr, Nd and Pb isotope geochemistry of Tertiary and Quarternary alkaline volcanics from West Germany. *Earth and Planetary Science Letters*, 79:107–119, 1986.
119. T.R. Worsley, R.D. Nance, and J.B. Moody. Tectonic cycles and the history of the Earth's biogeochemical and paleoceanographic record. *Paleoceanography*, 1:233–263, 1986.
120. D. Yamazaki and S.-I. Karato. Some mineral physics constraints on the rheology and geothermal structure of the Earth's lower mantle. *American Mineralogist*, 86:385–391, 2001.
121. W.-S. Yang. *Variable viscosity thermal convection at infinite Prandtl number in a thick spherical shell*. PhD thesis, University of Illinois, Urbana-Champaign, 1997.
122. D.A. Yuen, U. Hansen, W. Zhao, A.P. Vincent, and A.V. Malevsky. Hard turbulent thermal convection and thermal evolution of the mantle. *Journal of Geophysical Research*, 98:5355–5373, 1993.
123. D.A. Yuen and A.V. Malevsky. Strongly chaotic Newtonian and non-Newtonian mantle convection. In D.A. Yuen, editor, *Chaotic Processes in the Geological Sciences*, pages 71–88. Springer, New York, 1992.
124. A. Zindler and S. Hart. Chemical geodynamics. *Annu. Rev. Earth Planetary Sci.*, 14:493–571, 1986.